Matter and Radiation at Extremes

RESEARCH ARTICLE

pubs.aip.org/aip/mre

Controlled transition to different proton acceleration regimes: Near-critical-density plasmas driven by circularly polarized few-cycle pulses

Cite as: Matter Radiat. Extremes 8, 054001 (2023); doi: 10.1063/5.0151751
Submitted: 24 March 2023 • Accepted: 4 July 2023 •
Published Online: 27 July 2023

View Online Export Citation CrossMark

Shivani Choudhary De Marco,[1] Sudipta Mondal,[1] Daniele Margarone,[2] and Subhendu Kahaly[1,3,a)]

AFFILIATIONS

[1] ELI-ALPS, ELI-HU Non-Profit Ltd., Wolfgang Sandner utca 3, Szeged 6728, Hungary
[2] ELI Beamlines Center, Institute of Physics, Czech Academy of Sciences, Za Radnicí 835, 252-41 Dolní Břežany, Czech Republic
[3] Institute of Physics, University of Szeged, Dóm tér 9, H-6720 Szeged, Hungary

[a)] **Author to whom correspondence should be addressed:** subhendu.kahaly@eli-alps.hu

ABSTRACT

A controlled transition between two different ion acceleration mechanisms would pave the way to achieving different ion energies and spectral features within the same experimental set up, depending on the region of operation. Based on numerical simulations conducted over a wide range of experimentally achievable parameter space, reported here is a comprehensive investigation of the different facets of ion acceleration by relativistically intense circularly polarized laser pulses interacting with thin near-critical-density plasma targets. The results show that the plasma thickness, exponential density gradient, and laser frequency chirp can be controlled to switch the interaction from the transparent operating regime to the opaque one, thereby enabling the choice of a Maxwellian-like ion energy distribution with a cutoff energy in the relativistically transparent regime or a quasi-monoenergetic spectrum in the opaque regime. Next, it is established that a multispecies target configuration can be used effectively for optimal generation of quasi-monoenergetic ion bunches of a desired species. Finally, the feasibility is demonstrated for generating monoenergetic proton beams with energy peak at $\mathscr{E} \approx 20$–40 MeV and a narrow energy spread of $\Delta\mathscr{E}/\mathscr{E} \approx 18\%$–$28.6\%$ confined within a divergence angle of ~175 mrad at a reasonable laser peak intensity of $I_0 \simeq 5.4 \times 10^{20}$ W/cm^2.

© 2023 Author(s). All article content, except where otherwise noted, is licensed under a Creative Commons Attribution (CC BY) license (http://creativecommons.org/licenses/by/4.0/). https://doi.org/10.1063/5.0151751

I. INTRODUCTION

Advancements in modern targetry technology and a growing interest in near-critical-density (NCD) plasmas[1,2] using both gas-based[3–6] and solid-based[7–10] interaction have paved the way for a new regime of particle acceleration in relativistically intensity laser–plasma interactions. The advent of powerful ultrashort multicycle[11,12] and few-cycle laser facilities worldwide[13,14] along with sophisticated beamlines[15,16] makes such experiments feasible in the near future. Over several decades, the quest to achieve monoenergetic proton beams of megaelectronvolt energy has influenced the growth in research into laser-based particle acceleration,[17,18] due to their enormous potential for applications in materials[19] and medical sciences,[20–22] fusion schemes,[23,24] industrial applications,[25] and as neutron sources.[26]

Various ion acceleration processes have already been identified and demonstrated. For example, the most widely studied and investigated ion acceleration mechanism has been target normal sheath acceleration (TNSA),[27–29] which occurs predominantly when a high-intensity laser pulse interacts with an opaque solid-density thick foil target to produce a proton beam with maximum proton energy in the range of several tens of megaelectronvolts.[30,31] In this process, the hot electrons generated during the laser interaction transport through the target and exit from the rear end, creating a sheath electric field that accelerates the protons and other ions present at the back end layer of the target along the direction of target normal.[32] The main constraint with TNSA is the resulting broad energy spectrum, which makes it very challenging to use such beams for societal applications if beam conditioning (energy selection) is not implemented. Energy selection, on the other hand, reduces the ion

beam flux on a sample (i.e., a biological one), such as those in cancer therapy.[33]

An intense ultrashort laser pulse also imparts radiation pressure during the interaction, which is a function of the reflectivity of the relativistically exited foil target. The complete transmission of ultra-intense laser light from the plasma surface results in zero radiation pressure, whereas it is maximized in the case of complete reflection. In a typical laser–plasma interaction at relativistic intensity, the radiation pressure can reach nearly giga-bar (10^9 bar) level,[34,35] and under optimal conditions this can accelerate ions favorably. Radiation pressure acceleration (RPA) has been shown to operate in two different acceleration regimes, i.e., hole-boring (HB) RPA[35–37] (for micrometer-thick targets) and light-sail (LS) RPA[38,39] (for nanometer-thick targets), with distinct features in the resulting ion spectra. RPA has its own limitations, such as the fact that LS RPA works well only at ultrahigh intensities ($\gg 1 \times 10^{21}$ W/cm^2) and HB RPA requires long-pulse (of the order of picoseconds) high-energy lasers because a relatively long pulse time and large pulse energy are required to effectively drill a hole into the target[35] and to accelerate ions at the target front side via RPA. The maximum observed proton energy from a target in the RPA regime is ~48 MeV.[40]

Light reflection plays a crucial role in the relativistic interaction. In non-relativistic plasma, an incident laser pulse with frequency ω lower than the plasma frequency $\omega_p = \sqrt{n_e e^2/\varepsilon_0 m_e}$ (where n_e is the electron density of the target plasma, ε_0 is the vacuum permittivity, and e and m_e are the electron charge and mass, respectively) is reflected. The critical plasma density $n_c = m_e\omega^2\varepsilon_0/e^2$ at which the plasma frequency equals the wave frequency marks the transparency threshold, and for $n_e > n_c$, the plasma is described as overdense. For relativistically intense lasers, the plasma electrons are accelerated by the laser field lowering the effective critical density by a factor of $\langle\gamma\rangle$,[8,35,41,42] which is the average Lorentz factor of the electrons in the reflecting layer, increasing the transparency threshold to $n_c^{rel} \approx \langle\gamma\rangle n_c$.[42] Thus, the plasma becomes relativistically underdense for $n_e < n_c^{rel}$, and this is the relativistically induced transparency (RIT) regime that optically switches opaque plasma to transparent, enabling light propagation.[43–45] In recent years, several articles have reported efficient proton acceleration from ultra-thin nanometer-scale targets in this regime.[46–51]

Herein, via a series of fully relativistic 2D plane-wave particle-in-cell (PIC) simulations over a wide range of laser and target parameters, we demonstrate the possibility of transitioning between two different ion acceleration mechanisms, i.e., RIT and RPA. These ion acceleration regimes do not necessarily require petawatt-class lasers but potentially can be achieved using sub-petawatt peak power and moderate (~10^{20} W/cm^2) laser intensities. These parametric variations provide a route to effectively tune the spectral characteristics of the generated ions from the target. We investigate how the peak plasma density, target thickness, plasma density gradient, target geometry (double-layer configuration), laser temporal chirp, and laser focal-spot size influence the ion acceleration process from the NCD plasma. We have also identified the conditions that can effectively accelerate quasi-monoenergetic ions of a desired species with narrow energy spread. To access a wide range of available parameter space, we conducted more than 9000 quasi-1D (one space and three velocity) PIC simulations. Furthermore, to validate our results and to investigate multidimensional effects, we conducted several 2D PIC simulations. Therefore, the results presented herein are applicable to multidimensional situations with appropriate focusing conditions. Two-dimensional PIC simulations clearly unveil the underlying mechanisms behind the acceleration of monoenergetic ion species from a double-layer target, and the developed understanding could potentially be investigated experimentally at existing laser facilities such as ELI-ALPS,[13–15] ELI beamlines,[52] SIOM,[53] or other places in the world.[54]

This paper is structured as follows. In Sec. II, we discuss ion acceleration from foil NCD targets with a step-like density profile, and we highlight the distinctive features of the processes in both the transparent and opaque regime and in both real and phase space. In Sec. III, we summarize our observations on how target thickness and plasma density affect the transition to different proton acceleration regimes, and we investigate the robustness of the correlation between optical transparency and the nature of proton-energy spectral shape. In Sec. IV, we discuss the influence of an exponential density ramp in front of the foil target, a feature that can be controlled entirely optically in experiments with a pre-pulse. In Sec. V, we explore and summarize how temporal chirp affects the ion spectral characteristics for different target species, and in Sec. VI we show that a chosen ion species can be accelerated preferentially using a double-layer target. Finally, in Sec. VII we discuss the effects of dimensionality and focusing conditions on ion energy and on ion beam quality in the double-layer target configuration, and we probe deeper into quasi-monoenergetic ion acceleration.

II. PROTON ACCELERATION IN STEP-LIKE SUB-WAVELENGTH-SCALE NEAR-CRITICAL-DENSITY FOILS

To a large extent, the interaction of a relativistically intensity laser pulse with a semi-infinite plasma and the subsequent plasma dynamics can be modeled accurately using a 1D cold-fluid model.[55] In the reflection region (vacuum side), this theory provides the stationary solution at the vacuum–plasma boundary by balancing the ponderomotive and electrostatic forces. In the plasma side, the laser ponderomotive force pushes electrons inside the plasma to a new position leaving the immobile ions behind, and consequently a strong charge separation field is created that peaks at the new electron position. However, under the interaction condition, when most of the electrons escape from the target, the laser pulse starts to propagate deeper inside, thus the electron dynamics become more complex and the cold-fluid approximation ceases to be valid. Therefore, PIC simulations are required to understand the behavior of the interaction in this regime.

For a Gaussian laser pulse with elliptical polarization, the laser electric field $\mathbf{a}$ can be defined as

$$\mathbf{a}(\eta) = \frac{a_0 f(\eta)}{\sqrt{1+\varepsilon^2}}[\cos[\phi(\eta)]\mathbf{e_y} + \varepsilon \sin[\phi(\eta)]\mathbf{e_z}], \quad (1)$$

where the laser electric field $\mathbf{a}(\eta)$ is in units of $m_e\omega c/e$, $f(\eta) = \exp[-4\ln(2)\frac{\eta^2}{\tau_{FWHM}^2}]$ is the normalized pulse envelope function,

© Author(s) 2023

$\phi(\eta) = 2\pi\eta$ is the phase function, and $\eta = t - x$ is the propagation coordinate (where the space and time coordinates are normalized with respect to the time period τ corresponding to the central carrier frequency and the laser central wavelength λ, respectively). τ_{FWHM} is the FWHM of the time-dependent intensity envelope, and a_0 is the normalized laser pulse amplitude. Here, m_e and e are the mass and charge of the electron, respectively. ε is the ellipticity parameter, which can vary from −1 (left-handed circular polarization) to 0 (linear polarization) to +1 (right-handed circular polarization), where the sign determines the helicity and the magnitude defines the ellipticity in general. We kept $\varepsilon = -1$ for all the cases studied in the present investigation.

Furthermore, using 1D model equations, one can obtain the threshold limit for the self-induced transparency and differentiate between the regions of transparency and opacity for a semi-infinite overdense plasma target in the relativistic framework.[43,44] More rigorously, by using fully relativistic PIC simulations, one can obtain the percentages of laser pulse energy reflection and transmission from the target surface. In our study, we follow the second procedure, while conceptually benefiting from comparing the results with the expectations from the model. A constant parameter ξ_0 is taken into account that defines the normalized surface density of the target;[56] this is proportional to the product of the target density (n_e) and thickness (d) of the thin plasma slab and is given by $\xi_0 = \pi\left(\frac{n_e}{n_c}\right)_{\omega_0}\frac{d}{\lambda}$. In the case of moderate intensities $(a_0 < 1)$, $\xi_0 < 1$ corresponds to the transparency regime, whereas for ultra-intense laser pulses $(a_0 > 1)$ in the nonlinear regime, transparency is achieved when $\xi_0 > 1$ and $a_0 \geq \xi_0$ (or $a_0/\xi_0 \geq 1$).[56]

For a clear understanding of the regions of transparency and opacity, we used 2D plane-wave simulations with the fully relativistic PIC simulation code LPIC++[57] with modifications to the target conditions (e.g., introducing an additional layer and an exponential ramp) as well as implementing a Gaussian profile and chirp function in the laser. To investigate the role of peak plasma density n_{e0} for a given laser central frequency and foil thickness, we consider a quasi-neutral plasma foil with $n_e(x) = n_{e0}[H(x - x_1) - H(x - x_2)]$, where H is the Heaviside step function and $d = x_2 - x_1$ is the target thickness.

A CP laser pulse with normalized amplitude $a_0 = 20$ ($I_0 \simeq 5.4 \times 10^{20}$ W/cm^2) and a field envelope with an FWHM of five cycles is normally incident on the sharp-gradient plasma slab of thickness 0.75λ from the left side of the simulation domain of thickness 100λ with 140 cells per wavelength and 1500 particles per cell. The laser and target parameters are taken in dimensionless units, and space and time are normalized as x/λ and t/τ, respectively, where $\lambda = 1$ μm is the laser wavelength and $\tau = \lambda/c$. The electron density is normalized with respect to the critical density n_c, and the fields are normalized as $eE/m_e\omega c \to E$. The plasma slab is located at $35\lambda < x < 35.75\lambda$ with a density of $3n_c$ (which is considered as nominally overdense) for the intensity of ~5.4×10^{20} W/cm^2, hence we have $\xi \sim 7$ and therefore $\frac{a_0}{\xi} > 1$, thereby satisfying the transparency condition. On the other hand, $n_e = 9n_c$ is a fully overdense region for the given intensity and results in $\xi \sim 21.195$, where the ratio $\frac{a_0}{\xi} \lesssim 1$, therefore tapping into the total-reflection region.[38,58] This type of NCD is used in experiments involving foam targets,[59] cryogenic hydrogen jet targets,[60] and cryogenic solid hydrogen targets.[61] For such NCD and low-charge-state plasma interacting with short intense laser pulses, collisions can be neglected,[62,63] so collisions are not included in our PIC simulations.

Figure 1 shows the spatiotemporal profiles of the laser intensity and the electron and ion densities for the given laser and target parameters. Figures 1(a) and 1(c) show the two dynamically opposite cases with nearly 90% [Fig. 1(a)] and 0% [Fig. 1(c)] transmission of the laser pulse through the target. Therefore, for these two regions of ion acceleration, we refer to the nominally underdense region as *relativistic transparency* [Figs. 1(a) and 1(b)] and the overdense region as *opacity* [Figs. 1(c) and 1(d)].

For a linearly polarized laser pulse interacting with an overdense plasma slab, the 2ω oscillating part of the ponderomotive push

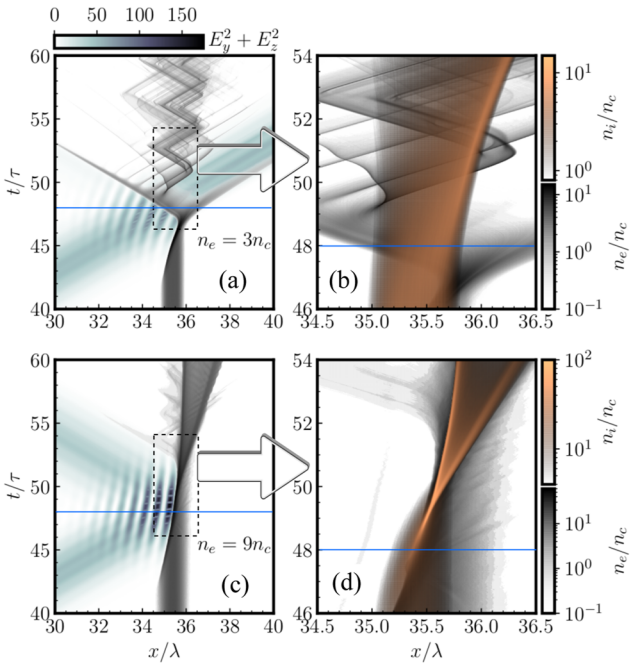

FIG. 1. Spatiotemporal dynamics of a thin slab target driven by an intense few-cycle circularly polarized (CP) electric field and with thickness in the sub-λ regime (in this case, a foil of thickness $d = 0.75\lambda$). The spatiotemporal evolutions of the laser intensity $E_y^2 + E_z^2$ (representing the incident, reflected, and transmitted light), electron density n_e, and ion density n_i are shown for two different initial plasma densities n_0 representative of the two distinct scenarios. The upper row [(a) and (b)] for $n_0 = n_e = 3n_c$ corresponds to the transmission regime, and the lower row [(c) and (d)] for $n_0 = n_e = 9n_c$ corresponds to complete reflection of light. The blue solid horizontal lines mark the instant $t = 48\tau$ when the peak of the pulse envelope interacts with the target surface. (b) and (d) show magnified views of the dashed boxes in (a) and (c), respectively, capturing the distinct signatures of the ion and electron dynamics in the two different regimes during the relativistic interaction. Both targets are initially overdense and reflect the laser (because $n_0 > n_c$), which interferes with the incident pulse to form a standing wave pattern in front of the target (see the intensity fringes on the front side of the target). (a) Near the peak of the pulse, the target becomes optically thin (dynamically underdense), pushing out electrons from the surface, initiating complex electron dynamics in the ion background, and expanding the ion density distribution shown in (b). (c) The target remains overdense within the laser pulse duration, leading to the synchronous motion of the electron and ion density peaks shown in (d). For both cases, we used a Gaussian laser pulse with normalized peak laser pulse amplitude $a_0 = 20$ [as in Eq. (1)].

© Author(s) 2023

introduces corresponding oscillations in the electron density. However, in the case of a normally incident CP laser pulse, a steady compression of the electron layer into the target[35,64] inhibits the $J \times B$ heating.[65] In the relativistic transparency region, as evident in Fig. 1(a), this ponderomotive push causes a sufficient number of electrons to escape from the target, thus leaving an underdense target near the peak of the CP pulse. As the laser pulse propagates through the target, the electrons in the vicinity of the laser field move both forward (target rear) and backward (target front), whereas being heavier in mass, the ions undergo a marginal expansion around the target surface (from 35λ to 35.75λ), mostly in the forward direction as shown in Fig. 1(b). The electrons that are removed from the target's ion background create a charge separation at the interface generating a strong electrostatic field. As a result, the electrons are pulled back to the target surface toward the ions and oscillate around the interface of the target. A magnified illustration of this process is shown in Fig. 1(b) with ion and electron density profiles. The horizontal blue lines in Fig. 1 mark the time at which the peak of the laser field interacts with the target. As seen in Fig. 1(a), as the rising part of the laser field interacts with the target, the ponderomotive force imparted by the laser field compresses the electrons into the ion background, eventually pushing out some of the electrons near the peak of the laser field leading to light transmission. Afterward, the remaining electrons oscillate back and forth in the ion background, leading to expansion of the ions as seen in Fig. 1(b).

The interaction in the opaque regime ($n_e = 9n_c$) is shown in Figs. 1(c) and 1(d). In Fig. 1(c), we see completely different electron dynamics. Because of the interaction of the CP laser pulse with the overdense target, most of the laser pulse is reflected. Therefore, all the electrons are compressed inside the target and are piled up at the rear side of the target leading to the formation of two electron bunches at a later time. For a clear view, Fig. 1(d) shows a magnified part of the spatiotemporal profiles of the electron and ion densities during the interaction, and we see that the positions of the electrons and ions closely overlap with each other and co-propagate, as shown in Ref. 2. At this point, we note that the partial transmission and reflection of the light field during the interaction is captured well in the color map presenting the intensity envelope in Figs. 1(a) and 1(b). A standing wave pattern is clearly visible in the target front side, representing the interference of the incident and reflected light fields and hence persisting only as long as the light reflection persists during the interaction. As seen in Fig. 1(a), near the blue line, the target becomes partially transparent, reducing thereafter the contrast in the standing wave pattern.

To discuss the underlying physics behind the ion acceleration in these two specific regions of interest, Fig. 2 shows the transverse and longitudinal electric fields along with the ion and electron density profiles for the aforementioned laser intensity and target density cases. Here, we consider two specific time instants, one at $t = 48\tau$, when the peak of the driver pulse interacts with the target, and another at $t = 70\tau$, which we call post-interaction. At these two

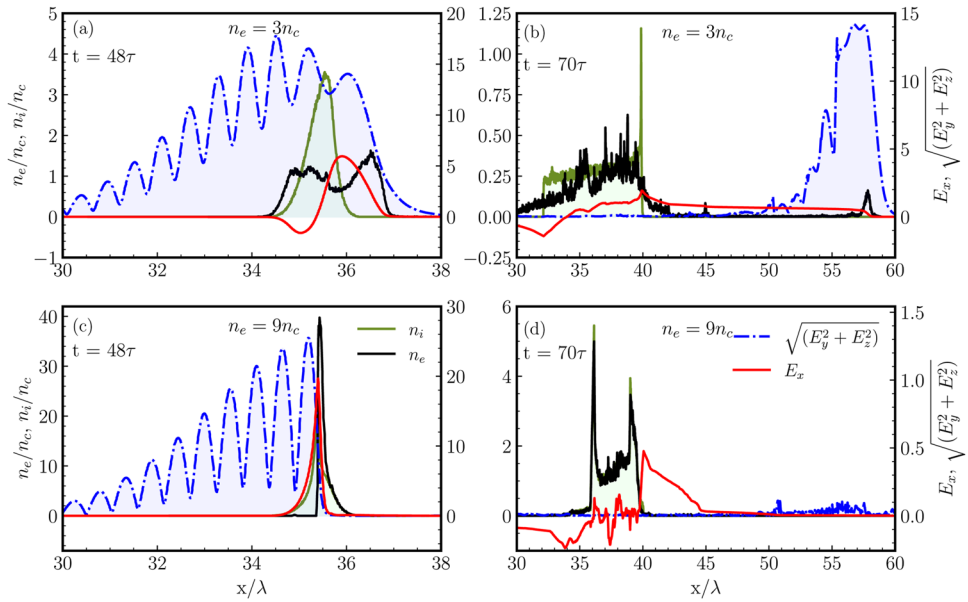

FIG. 2. Temporal snapshots showing profiles of driver laser field magnitude (dashed blue line representing incident, reflected, and transmitted fields), longitudinal electric field (red solid line representing accelerating field), ion density (green solid line), and electron density (black solid line) for the two scenarios: (a) and (b) are for $n_e = 3n_c$ (relativistic transparency regime), and (c) and (d) are for $n_e = 9n_c$ (overdense regime). For each case, the fields and densities are plotted at two different times: (a) and (c) are for time $t = 48\tau$, when the peak of the laser pulse is interacting with the target, and (b) and (d) are for the later time $t = 70\tau$, long after the driving field has ceased to interact with the target. Near the peak of the interaction, the target with lower initial density has already started to transmit the incident laser pulse, which can be seen in the blue shaded part on the right side of the target in (a) and is clearly captured after the interaction in the laser pulse co-propagating to the right along with the electron bunch as seen in (b). No such transmission can be seen in (c) and (d) [note the significantly small scale used for plotting the magnitude on the right axis for the radial electric field presented in (d)].

© Author(s) 2023

time instances, we analyze the behavior of all the field and density components.

In the relativistic transparency region at $t = 48\tau$ in Fig. 2(a), the laser pulse energy starts to propagate through the target with limited laser energy reflected. This eventually leads to the formation of a standing wave pattern of low contrast at the front side of the target as mentioned before. As discussed in the context of Figs. 1(a) and 1(b), because of the formation of the electron bunches on both sides of the target, a bipolar electrostatic field [five arbitrary units (AU)] is generated (red solid line) at $t = 48\tau$ that is the signature of target expansion on both sides. At a similar moment, a completely different behavior is observed for the opaque regime [Fig. 2(c)], which exhibits a unipolar longitudinal field. In this case, a substantial amount of laser energy is reflected from the target front surface, which leads to the formation of standing waves with high contrast. Therefore, the electrons receive a laser push in the forward direction in the form of radiation pressure and move inside the target, followed by the slowly moving ions, thus creating a charge separation only at the rear side of the target[66] and hence resulting in a unipolar electrostatic field (20 AU), as shown by the red curve in Fig. 2(c).

At a post-interaction time ($t = 70\tau$), we observe a strong persistent longitudinal electrostatic field in the relativistic transparency region as shown in Fig. 2(b). In this case, the laser pulse has already propagated through the target, and some of the electrons are expelled from the target to make it positively charged, which results in the ions expanding under Coulomb repulsion. A small fraction of electrons with very high energy nearly co-propagate with the transmitted laser pulse (as can be seen at 57λ), leading to the formation of a strong electrostatic field (two AU). Because the electrons escape from the target in both directions, this results in the generation of a negative electrostatic field at the target front.

In the case of the overdense target, as seen in Fig. 2(d), at the later time instant of 70τ, when the whole laser pulse has interacted with the target, the ions and electrons move nearly together forming an overlapping double peak structure in space. This results in the generation of a weak electrostatic field of ~0.5 AU. These bunches slowly expand in the target forward direction (rear side) under radiation pressure acceleration. This shows that the laser pulse transfers its momentum to the electrons and ions and lets them evolve under this momentum transfer.[67,68] Similar to the cold-fluid model, the position of the maximum electrostatic field is at the minimum of the electron density, as shown in Fig. 2(c) at the peak interaction of the pulse. At the later instant (70τ), the position of the peak electrostatic field cannot be interpreted correctly from the cold-fluid model, and this difficulty arises from ions being mobile and electron bunches leaving and re-entering the target, as mentioned in Ref. 43.

As shown earlier in Fig. 1(a) and elaborated in Fig. 2(a), the target with peak electron density $n_e = 3n_c$ becomes transparent near the peak of the laser field. On the other hand, for the target with peak electron density $n_e = 9n_c$ [as shown in Figs. 1(c) and 2(c)], the laser field fails to pass through the target even at the peak of the field envelope. To investigate the ion dynamics in more detail and to

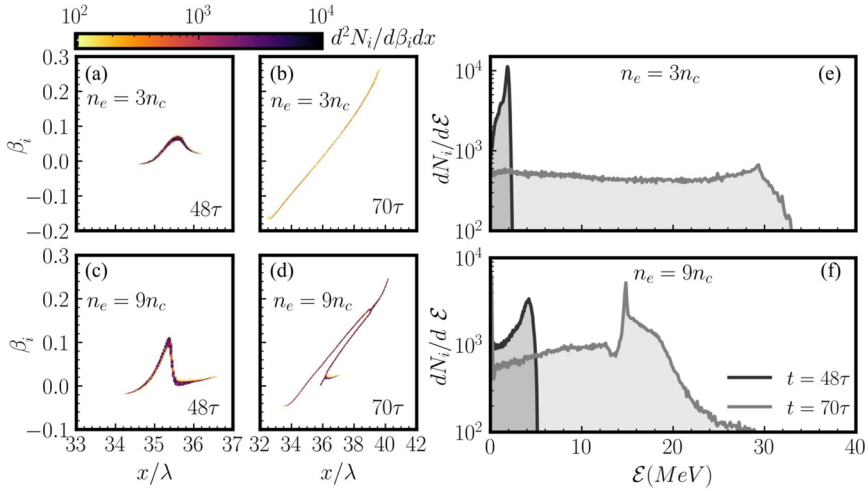

FIG. 3. Temporal snapshots of ion phase-space distribution and corresponding energy spectra. (a) and (b) Ion phase-space distribution in blow-out regime ($n_e = 3n_c$) of interaction at two different time instants. (c) and (d) Ion phase-space distribution in opaque regime ($n_e = 9n_c$) of interaction at the same time instants. At $t = 48\tau$, the laser pulse peak is interacting with the target, whereas $t = 70\tau$ is long after the driving field has ceased to interact with the target. The color bar for (a)–(d) represents the number of macroparticles $d^2N_i/d\beta_i dx$ accelerated in the laser propagation direction with velocity (β_i), normalized by the speed of light in vacuum (c), per unit bin in the phase space. (e) and (f) Ion energy spectra $dN_i/d\mathscr{E}$ corresponding to the interactions represented in (a)–(d). Both targets behave in a reflective manner until near the peak of the laser pulse envelope reached at $t = 48\tau$. At the peak of the driving field, the foil with $n_e = 3n_c$ becomes transparent, whereas the one with $n_e = 9n_c$ remains reflective during the whole relativistic interaction. The two different behaviors representative of the two different regimes of operation are captured very well in this figure. During the reflective regime, the phase-space velocity distributions in (a), (c), and (d) have similar folded shapes and peaky features that become significantly different in (b) once the interaction enters the transparent regime, and the aforementioned similar behavior is a signature in the ion energy spectra. For the reflective part of the interaction [dark shaded curves in (e) and (d)], the ion energy spectra show distinct quasi-monoenergetic behavior that is retained even after the interaction is over, as seen in the light shaded curve in (f), but that erodes away once the target enters the transparent regime even partially, as seen in the light shaded curve in (e).

© Author(s) 2023

identify the differences between the regimes of transparency and opacity, we now analyze the phase-space data and look into the behavior of the ions in the aforementioned cases in Fig. 3. The ion velocity in the direction of laser incidence (along decreasing x) in units of c is represented by β_i in the color map, where positive β_i in Fig. 3 indicates ion velocity into the target (from left to right in Figs. 1 and 2). Before the peak of the laser pulse interacts with the target, in both cases the target remains predominantly reflective, as is evident from the relatively high contrast of the interference fringes in the front side of the target [Figs. 2(a) and 2(c)]. From the beginning of the interaction until this time, the electrons face the increasing Lorentz push from the laser field and gain energy, which is self-consistently transferred to the ions via the plasma charge separation field. As is evident in Fig. 3(a), for the target that eventually becomes transparent at the peak interaction (48τ), the ions gain in forward momentum, showing a β_i peak located at $x = 35.75\lambda$ (which is inside the initial target surface at $x = 35\lambda$) in the phase-space velocity distribution. Note here that the asymmetric bipolar charge separation field E_x [the different values of the negative and positive peaks in the red curve in Fig. 2(a)] leads to the asymmetric ion velocity distribution in Fig. 3(a), being skewed toward the laser propagation direction. Long after the interaction (at 70τ) in the transparent target, as shown in the phase-space distribution in Fig. 3(b), we see that ions have expanded in both directions (front and rear), with a slower ion expansion at the front side of the target (having a velocity cutoff near $\beta_i \sim 0.18$) than at the rear side (having a velocity cutoff near $\beta_i \sim 0.27$). In this case, because the ions undergo Coulomb repulsion, they expand in both directions (front and rear) as in Fig. 1(b).

Note here that if the features of the ion velocity distribution are closely linked with the regimes of transparency during the interaction, then at this point one might expect that until $t = 48\tau$ both targets should show qualitatively similar ion phase-space behavior. This behavior is fully corroborated by the similar features observed in the opaque region, as shown in Fig. 3(c), near the peak of the pulse. However, there are few qualitative differences regarding the scenario in Fig. 3(a). First, in Fig. 3(c) we see that at $t = 48\tau$, the peak of the β_i distribution is located at a higher value compared to the previous case. Second, in the case of $n_e = 9n_c$, the asymmetric phase-space ion velocity distribution is more skewed. Both these points can be understood well by looking at the E_x field profile in Fig. 2(c), which shows a higher value of peak field and a sharper field profile inside the target than in the front side. Therefore, the ions show some expansion at the target front but are much more piled up within the target thickness, thereby showcasing the buildup of charge as shown in Fig. 3(c). At a longer time delay after the interaction $(t = 70\tau)$, for the opaque region [Fig. 3(d)], we observe two distinct ion velocity distributions, with one ion bunch accelerating from the front surface of the target and another accelerating from the rear surface of the target. Eventually, both ion bunches merge to form a single ion distribution at $x = 39\lambda$.

Now we look at the nature of the ion energy spectra for the ions moving in the direction of laser incidence. The ion energy spectra when the peak of the laser pulse interacts with the target $(t = 48\tau)$ are shown in black in Figs. 3(e) and 3(f) for both cases (transparent and opaque). The ion energy peaks and then experiences a sharp cutoff, which is typical spectral behavior of HB RPA.[69] Because before $t = 48\tau$ (peak interaction) the interaction is not yet over and transparency is not achieved, both target conditions are in an overdense region, where we see the spectral signature of the opaque region. At this intermediate interaction time, the ion cutoff energy is higher in the opaque region [Fig. 3(f)] than in the transparent case [Fig. 3(e)] because of the higher accelerating field operating at that instant. Also, during the post-interaction phase (70τ), in the transparency region [Fig. 3(e)], the accelerated ions follow a Plataea structure with peak energy of ~30 MeV, whereas there is quasi-monoenergetic behavior in the opaque region [Fig. 3(f)] with peak ion energy of ~16 MeV. The peak ion energy from the transparent region and the cutoff ion energy from the opaque region are ~30 MeV in these particular cases. Note that the respective ion energy spectra presented here correspond to spatially integrated velocity distributions at the relevant moments. Therefore, in this section we have discussed the typical features of the interaction, the ion and electron density distributions in the real spatiotemporal domain, the relevant accelerating fields during and after the interaction, and their consequences for the ion phase-space distributions and resulting ion energy distributions for two special cases of interest. This has helped us to identify the signatures of the two different regimes of interaction. In the following, we undertake a more systematic study of the effects of different target and laser parameters on the ion acceleration process in our regimes of interest, trying to decipher the generic features that would allow us to design and establish an approach relevant for experiments.

III. INFLUENCE OF FOIL THICKNESS AND PEAK PLASMA DENSITY: TRANSITION BETWEEN ACCELERATION REGIMES

In this section, we investigate how varying the thickness of the foil target affects the ion acceleration mechanisms of RIT and RPA. In Ref. 43, the stationary solutions for the 1D scenario were derived assuming the validity of the cold-fluid model, which assumes a CP monochromatic laser pulse interacting with overdense plasma with a step-like electron density profile in a background of immobile ions. In the context of the cold-fluid model, at this point we define a threshold electron density of the target (n_{th}). The threshold density is the maximum electron density that allows the laser pulse to transmit through the plasma target. The scaling law for the threshold density was given in Ref. 45 in the case of a relativistic intense laser pulse $(a_0 \gg 1)$ incident on a semi-infinite plasma slab. A modified expression for the threshold density incorporating the effect of target thickness was presented previously in a phenomenological way in Ref. 58 as

$$n_{th} \sim \frac{2\lambda}{9d}\left(3 + \sqrt{9\sqrt{6}a_0 - 12}\right)n_c. \tag{2}$$

In the following, we use this expression as a reference model, and we check its validity via a comparative study of a large number of PIC simulations. In this context, as a first step, we must define clearly what we mean by transparent and opaque regimes over our parameter space of interaction.

To define the transparent and opaque regimes more quantitatively and consistently, we define a parameter $\mathscr{E}_t$ known as the transmitted energy fraction, i.e.,

$$\mathscr{E}_t = \frac{\int_{\eta_i}^{\eta_f} (E_y^2 + E_z^2)|_{TF}\, d\eta}{\int_{\eta_0}^{\eta_i} (E_y^2 + E_z^2)|_{IF}\, d\eta}, \tag{3}$$

© Author(s) 2023

where E_y and E_z are the transverse components of the propagating laser field, and η_0, η_i, and η_f are the respective spatiotemporal representations for before (interaction has not started), beginning (initiation of interaction), and end (interaction is over) of the interaction regions. Here, $\eta = t - x$ (t and x are in units of τ and λ, respectively, implying $c = 1$), and the suffixes IF and TF correspond to the incident and transmitted fields, respectively. In simulation time, we have $\eta_0 = 0$, $\eta_i = 36\tau$, and $\eta_f = 60\tau$. In Eq. (3), the numerator $\int_{\eta_i}^{\eta_f}(E_y^2 + E_z^2)|_{TF}$ represents the transmitted fluence after the interaction with the target is over, and the denominator $\int_{\eta_0}^{\eta_i}(E_y^2 + E_z^2)|_{IF}d\eta$ indicates the incident laser fluence on the target, both expressed in the same units. Thus, here we have defined the transmitted energy fraction as the ratio between the transmitted laser energy and the incident laser energy. This parameter is calculated directly by post-processing the PIC simulation results. For given target and laser parameters, $\mathscr{E}_t = 1$ implies total transmission and $\mathscr{E}_t = 0$ indicates no transmission at all, implying that the laser energy is either totally reflected or absorbed. In a real interaction, the value of the parameter lies between these two extremes, i.e., $0 \leq \mathscr{E}_t \leq 1$. Thus, using the criterion of the transmitted energy fraction $\mathscr{E}_t$ of the laser pulse, we can differentiate between the regions of transparency and opacity in a quantitative manner.

The color map in Fig. 4(a) shows the variation of the transmitted energy fraction $\mathscr{E}_t$ when the interaction spans a range of target peak electron density $n_e/n_c \in [2, 10]$ and a sequence of target thickness $d/\lambda \in [0.75, 1.55]$ at each peak electron density. To begin with, each combination of target peak plasma electron density and target

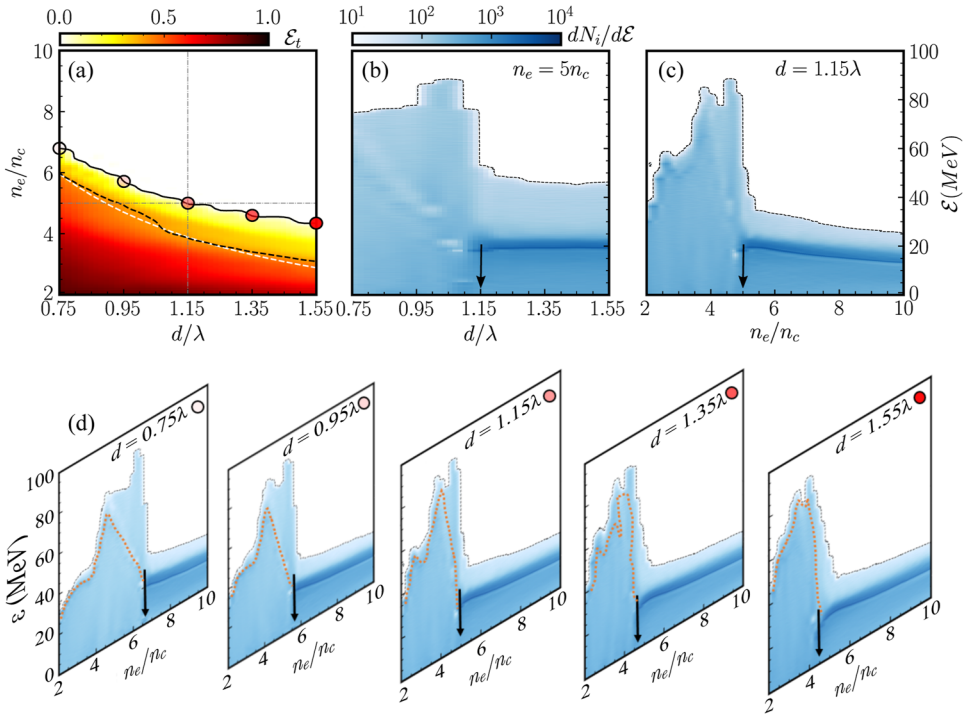

FIG. 4. Correlation between interaction regime and nature of resulting ion energy spectra: step-density targets. (a) Fraction of laser energy transmitted through target with varying thickness (d/λ) and peak electron density (n_e/n_c) at simulation time 70τ. The 2% (black solid line) and 40% (black dashed line) transmitted energy fractions are shown, with the 40% black dashed line indicating the threshold target density (n_{th}) for relativistically induced transparency (RIT) for varying target thickness. The analytically predicted threshold target density [Eq. (2)] is shown with a white dashed line and is consistent with the 40% iso-line obtained from particle-in-cell (PIC) simulations. The color bar shows the laser pulse energy transmission coefficient $(\mathscr{E}_t)$ as in Eq. (3). The target density $n_e = 5n_c$ and thickness $d = 1.15\lambda$ are marked with horizontal and vertical gray lines in (a). In (b), the ion energy spectral map with varying target thickness is presented for the threshold density of $n_e = 5n_c$ [along the horizontal iso-density gray dashed line in (a)]. In (c), the ion energy spectral map for the target thickness of $d = 1.15\lambda$ is presented with varying target density [along the vertical iso-thickness gray dashed line in (a)]. Note that the color map for ion energy is plotted in logarithmic scale. The spectral map in (b) and (c) shows unequivocally that as the interaction enters from transparency into the opaque regime [across the 2% iso-transparency black solid curve in (a)], the accelerated ion energy spectra goes from exponential to quasi-monoenergetic peak structures irrespective of whether it is along the iso-density line or along the iso-thickness line. This establishes a consistent correlation between the regime of interaction and the nature of ion energy spectra over a wide range of parameter space. To probe this point further, we plot the ion energy spectral map along different iso-thickness lines with varying peak target density. (d) Shows the ion energy spectral map iso-thickness lines through the red semitransparent circles in the black curve separating the transparent and opaque regimes in (a). The black dotted lines in (b)–(d) represent the cutoff ion energy in both regions, whereas the orange dashed contour lines in (d) mark the peak ion energy in the relativistic transparency region. The black arrows in the ion energy spectral maps in (b)–(d) mark the interaction conditions corresponding to the $(n_e/n_c, d/\lambda)$ pairs on the black solid curve in (a) [identifying with the target conditions indicated by each circle shown in (a)] emphasizing the transition phase between the regimes, i.e., from transparent to opaque conditions through the 2% iso-transmission curve. A clear correlation can be seen between $\mathscr{E}_t$ and d. The color bar above (b) shows the number of ions accelerated and represents (b)–(d). All the spectra are for time 70τ.

© Author(s) 2023

thickness corresponds to a nominally overdense regime, implying complete light reflection in the case of a nonrelativistic laser peak intensity from the plasma critical density layer n_c. At our laser peak intensity, relativistic effects come into play. For the given laser parameters, interaction on this 2D target parameter space clearly brings out several features. First, along any vertical (increasing target peak electron density along a line of constant target thickness) or horizontal (increasing target thickness along a line of constant peak electron density) line on the color map in Fig. 4(a), the target becomes more reflective. Second, there is a clearly demarcated opaque region in the 2D parameter space along with a gradually increasing transparent regime. To define the transparency threshold, we define an iso-line at $\mathscr{E}_t = 0.02$ below which we consider the target to be transparent. Thus, the black solid iso-line marked at 2% transmitted energy fraction indicates the maximum limit in threshold density (n_{th}) for the laser pulse to undergo transmission or reflection from the target. The 40% black dashed iso-line of transmitted energy fraction shows remarkable matching with the variation of threshold density obtained under the cold-fluid approximation (the white dashed curve) using Eq. (2). Figure 4(a) shows that when the target thickness (d/λ) is approximately doubled, the threshold density (n_{th}) halves, i.e., from $6n_c$ at 0.75λ to $3n_c$ at 1.55λ. Increasing the target thickness (from 0.75λ to 1.55λ) and density (from $2n_c$ to $10n_c$) increases the target areal density $(\propto n_e d)$. Therefore, the incident laser field on the target is insufficient to remove a substantial amount of electrons from the target to achieve RIT and thereby reflect the pulse from the surface of the thicker target with higher electron density. This regime of ion acceleration lies under HB RPA. Thus, one can effectively control the transition from transparency to opacity by tuning the target thickness and density.

We now investigate the correlation between interaction regime and the nature of the ion energy spectra to see whether the understanding developed in Sec. II for two specific cases can be validated over a wider parameter range. To elucidate this process of transition, we present the ion energy spectral map in Fig. 4(b) at a fixed electron density $(n_e = 5n_c)$ and varying target thickness (d/λ). In this case, the target density is chosen in such a way that it can cover both regions, i.e., transparent (RIT) and opaque (RPA), over the range of target thickness [along the horizontal gray dashed line in Fig. 4(a)]. For the first half of the thickness variation (i.e., for $d < 1.15\lambda$), the condition satisfies RIT where the cutoff energy reaches a maximum of up to 90 MeV following the energy distribution as previously observed in Fig. 3(e). On the other hand, for target thicknesses of $d > 1.15\lambda$, a quasi-monoenergetic spectrum is observed akin to that in Fig. 3(f), with the constant peak ion energy peak at 20 MeV and cutoff energy of ~55 MeV. It is evident from Fig. 4(a) as well that for $n_e = 5n_c$, the iso-density line crosses the transparency threshold curve $(\mathscr{E}_t = 0.02)$ at $d = 1.15\lambda$, and the target starts to become opaque for all thicknesses $d > 1.15\lambda$. Therefore, we can refer to the thickness $d = 1.15\lambda$ as a transition thickness between these two regimes. This point representing the change in the ion spectra is marked with an arrow in Fig. 4(b).

Similarly, Fig. 4(c) shows the ion energy spectral map for fixed target thickness $(d = 1.15\lambda)$ while increasing the target density from $2n_c$ to $10n_c$. We observe similar behavior in the ion energy spectrum as in the case of the fixed-density $(5n_c)$ target shown in Fig. 4(b). Because $n_e = 5n_c$ is the threshold density (marked with an arrow) for the target thickness of 1.15λ, it acts as a transitioning density point. For $n_e < 5n_c$, the target undergoes transparency, and we observe the representative ion energy spectrum with cutoff energy increasing from 40 MeV for the target with near-critical density to 90 MeV for the target with higher density. By contrast, for $n_e > 5n_c$, the spectral features highlight quasi-monoenergetic behavior. However, in this case, we observe the reduced cutoff energy from 40 MeV (threshold density $n_e = 5n_c$) to 25 MeV (overdense target $n_e = 10n_c$) as well as peak ion energy from 20 to 15 MeV. Because the target densities $n_e > 5n_c$ are in the opaque region, the laser ponderomotive push is not strong enough to remove all the electrons from the target, resulting in a weak accelerating field that consequently restricts the ion energies within a certain limit.

In addition, in Fig. 4(d) we present the ion energy spectral map with varying target density for four different target thicknesses corresponding to those indicated with circles filled in different shades of red lying on the threshold density curve in Fig. 4(a). These exhibit the typical nature of the energy distribution in the transparent region (RIT) and quasi-monoenergetic distribution of the ion energy spectrum in the reflected regime (RPA). For each target thickness, the threshold density acts as a transitioning point, which is consistent with the transmitted energy fraction iso-line (2%) in Fig. 4(a). Additionally, we see that the peak ion energy (yellow dashed in transparent region and dark blue in opaque region) follows a similar trend to that of the ion cutoff energies (black dotted lines) for all the target thicknesses over the varying target density $(2n_c$ to $10n_c)$.

Therefore, the maximum ion cutoff energy at the target threshold densities for all the target thicknesses (0.75λ, 0.95λ, 1.15λ, 1.35λ, and 1.55λ) reaches 90 MeV. Also, the maximum ion cutoff energy is obtained in the RIT domain, ranging from ~40 to ~90 MeV, which is significantly higher than that achieved in HB RPA (~25 to ~40 MeV). In other words, the transition point between the RIT and RPA regimes is the key criterion for achieving maximum ion energy, where RIT determines the maximum ion cutoff energy and the HB-RPA region is the criterion for achieving quasi-monoenergetic peak ion energy (maximum ~20 MeV). Hence, one can benefit from the transition between different regimes of ion acceleration depending on the ion energy requirement for the given the experimental conditions.

IV. CONTROLLING PROTON ACCELERATION: FOIL WITH PLASMA DENSITY GRADIENT

In a realistic experimental scenario, the driving laser pulse always has a limited temporal contrast, which expands the target front surface and gives rise to the plasma gradient before the peak of the main laser is incident on the target. For the thin targets that are essential for applications involving ion acceleration with mechanisms such as HB[70] or relativistic transparency,[46] if the laser contrast is poor, then the target can be destroyed before the peak of the laser pulse can interact with it. The influence of pulse temporal contrast on the acceleration process in the case of optically thicker targets has been observed experimentally.[71] Thus, in all these experiments, the prerequisites are (i) high temporal contrast (typically $\geq 10^{-12}$) of

© Author(s) 2023

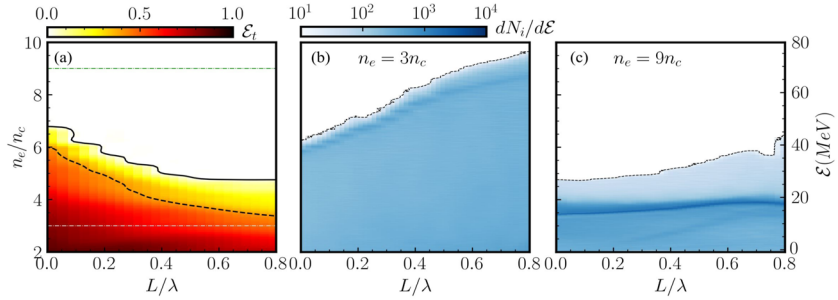

FIG. 5. Correlation between interaction regime and nature of resulting ion energy spectra: foils with varying plasma gradient scale lengths. (a) Fraction of transmitted laser energy for varying plasma scale length (L/λ) and density (n_e/n_c). The color bar shows the energy transmission coefficient $(\mathscr{E}_t)$ as defined in Eq. (3). The black solid line corresponds to 2% transmitted energy fraction, and the black dashed line corresponds to 40% transmitted energy fraction. (b) and (c) show the ion energy spectral maps with varying scale lengths for $n_e = 3n_c$ [dashed white line (a)] and $9n_c$ [dashed green line (a)], respectively. The black dashed contour lines in (b) and (c) mark the maximum or cutoff ion energy in each case. The color bar on top of (b) represents the number of particles accelerated per energy bin at the corresponding energy.

the main interacting laser and (ii) separate fine control of the target plasma density gradient.[72] Thus the impact of plasma density gradient on the physics under discussion cannot be overemphasized. In this section, we investigate how the plasma density gradient influences the ion acceleration process.

In this study, we used a 0.75λ-thick foil target with an exponential density profile $n(x) = n_0 \exp(-(x-35)/L)$ at the front side of the target as an extra controlling parameter for the interaction, where n_0 and L are the peak electron density and plasma scale length, respectively. In Fig. 5(a), we vary the target peak electron density and the plasma density scale length (L/λ) and plot the transmitted energy fraction as a function of these two parameters. Altering the target density gradient significantly affects the threshold density criteria. Similar to the case of thickness variation for the step target density profile, here as well we sketch iso-lines along the different scale lengths for 2% and 40% of light energy transmission through the target. With increasing scale length, the transmitted energy fraction of the laser pulse decreases for a fixed laser intensity. Subsequently, the target threshold density (n_{th}) reduces by ~30% because of the increase in overall areal density of the target. Also, we observe that the iso-lines (2% and 40%) for the case of varying scale length [Fig. 5(a)] show slightly higher threshold density compared with the case of step-like target thickness variation [Fig. 4(a)].

Furthermore, Figs. 5(b) and 5(c) show the spectral features of ion energy as a function of scale length for the relativistic transparency [$n_e = 3n_c$ marked with the white dashed line in Fig. 5(a)] and overdense [$n_e = 9n_c$ marked with the green dashed line in Fig. 5(a)] regions, respectively. In Fig. 5(b), the ion energy spectra show features similar to those in Fig. 3(e). In this case, the ion cutoff energy increases almost linearly from ~45 to ~80 MeV with increasing scale length. The peak ion energy increases from ~40 to ~65 MeV, closely following the behavior of the cutoff energy. On the other hand, in Fig. 5(c), the ion energy spectrum in the overdense region $(n_e = 9n_c)$ shows a significantly low increase in the ion cutoff energy from ~30 to ~40 MeV over the entire range of target scale length. However, the peak ion energy is maintained at nearly ~19 MeV with energy spread $\Delta\mathscr{E}/\mathscr{E} \sim 2.8\%$ for sharp gradient $(L/\lambda = 0)$ and 7.4% for long gradient $(L/\lambda = 0.80)$, where $\mathscr{E}$ is the peak ion energy and $\Delta\mathscr{E}$ is the FWHM of the peak energy. This highlights the quasi-monoenergetic feature from the overdense plasma target. In addition, for a fixed scale length, if we scan the target density (from $2n_c$ to $10n_c$), then we can transit from transparency to opacity interchangeably in a continuous manner, thus changing the ion energy spectrum to the quasi-monoenergetic distribution. Therefore, controlling L/λ is essential for controlling the ion energy distribution and acts as an extra optimization parameter for producing energetic protons.

Experimentally, controlling L/λ is done very easily by controlling the delay of a pre-pulse arriving before the main pulse starts interacting with the target. Optimizing pre-plasma using a pre-pulse has been used routinely in several experiments. The pre-pulse can be extracted from the main pulse by using a holey mirror[15,73] or by picking up a small portion of the main beam with a small mirror,[72,74] and the delay can be controlled with a separate delay stage.

V. CHIRP CONTROL OF FOIL DYNAMICS ON GRADIENT TARGET

In addition to controlling the target plasma characteristics, the ion acceleration in laser–plasma interaction can be optimized greatly by tuning the optical parameters of the drive laser.[75–78] The influences of laser polarization, pulse duration, and peak intensity under different target conditions have been touched upon previously,[38,47,79–82] and the potential of the relativistic transparency regime has been demonstrated experimentally.[50,83] Here, we introduce a frequency chirp in the driver pulse, which is relatively easy to control in an experiment, and we investigate how it affects the acceleration process. The frequency chirp is introduced within the phase function $\phi(\eta) = 2\pi[\eta + g(\eta,\zeta)]$ in the expression for the laser field in Eq. (1), where the chirp function $g(\eta,\zeta)$ is defined as

$$g(\eta,\zeta) = \left(\zeta\left[4\ln(2)\frac{\eta^2}{\tau_{FWHM}^2} + \frac{\pi^2\tau_{FWHM}^2}{4\ln(2)(1+\zeta^2)}\right] + \frac{\tan^{-1}(\zeta)}{2}\right)\frac{1}{2\pi}, \quad (4)$$

© Author(s) 2023

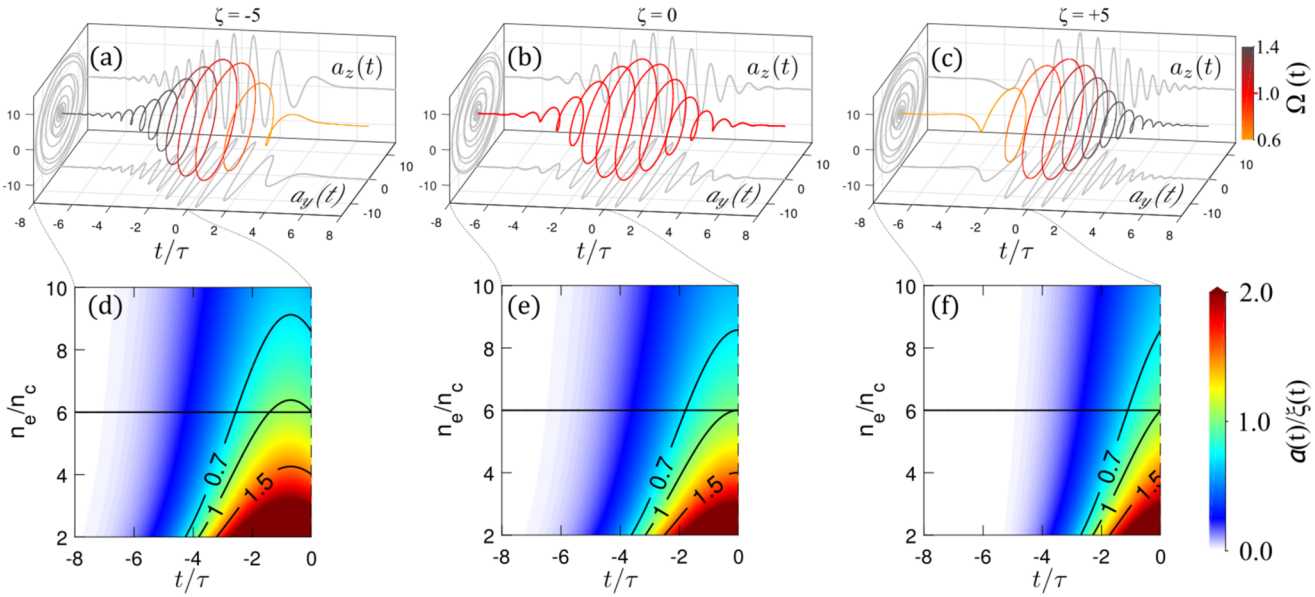

FIG. 6. A simplified picture illustrating the influence of laser chirp. Upper panels: temporal profiles of a circularly polarized (a) negatively chirped ($\zeta = -5$), (b) unchirped ($\zeta = 0$), and (c) positively chirped ($\zeta = +5$) laser pulse. The projected transverse field components $a_y(t)$ and $a_z(t)$ are presented as gray solid lines plotted on the respective transverse planes. The variation in time-dependent frequency of the laser pulse as shown in the color bar [$\Omega(t)$ as defined in Eq. (5)] is encoded on the color variation across the circularly polarized laser field. The pulse peak here is located at $t = 0$. $\Omega(t) = 1$ represents the carrier frequency, and negative t indicates early in the interaction. Lower panels: color maps of ratio of time-dependent laser pulse amplitude $a(t)$ and parameter $\xi(t)$ [defined in Eq. (6)] during first half of interaction (the time axis covers the range from the start of the laser pulse at -8τ to the peak of the pulse intensity at $t = 0$) for the step target case over a range of target densities for (d) negatively chirped, (e) unchirped, and (f) positively chirped pulse scenarios. The black contour lines are plotted at $a(t)/\xi(t) = 0.7$ (in opaque region), 1.0 (in threshold region), and 1.5 (in transparent region) for the fixed density case of $n_e = 6n_c$ (black horizontal solid line). As is evident, if the target remains unchanged during the interaction, then in (d) for the negatively chirped case, before the peak of the laser pulse intensity, the interaction at an initial target density of $n_e = 6n_c$ enters the transparent regime of operation. (e) The transparent regime is approached near the peak of the pulse for $\zeta = 0$, and (f) the same target meets the transparency condition after the peak of the laser pulse for $\zeta = +5$.

where ζ is the chirp parameter, and $\Omega(\eta)$ is the instantaneous frequency given by

$$\Omega(\eta) = \frac{1}{2\pi}\frac{\partial\phi(\eta)}{\partial\eta} = 1 + \frac{\partial g(\eta,\zeta)}{\partial\eta} = 1 + \zeta\frac{4\ln(2)}{\pi\tau_{FWHM}^2}\eta. \quad (5)$$

In these units, $\Omega = 1$ represents the central (at the peak of the pulse) carrier frequency of the pulse in the unchirped ($\zeta = 0$) case. This functional definition was first proposed in Ref. 77 as a chirped plane-wave model. However, a modification is made to take advantage of preserving the peak field amplitude of the pulse during any variation in the chirp.[78] This is done to ensure that when we investigate how the chirp parameter ζ affects the interaction, we can keep the other laser parameters fixed. To simplify the representation, in the following discussion we interchange η with t in the expressions without any loss of generality.

With the chirped Gaussian pulse defined above, we modified the PIC code to incorporate such a CP field and then performed a series of simulations to investigate how frequency chirp affects ion acceleration. Figure 6 shows the (a) negatively chirped, (b) unchirped, and (c) positively chirped laser pulses used in the simulation. The time-dependent instantaneous frequency of the pulse $[\Omega(t)]$ is shown with the color axis Figs. 6(a)–Figs. 6(c). In these particular plots, the peak of the laser field envelope is located at $t = 0$, and negative time indicates earlier in the interaction. The chirp is defined in such a way so that for a negatively (resp. positively) chirped pulse, the high-frequency (resp. low-frequency) components interact with the target first, followed by the low-frequency (resp. high-frequency) components.

Before we delve into the results of the fully relativistic PIC simulations, we discuss here pedagogically the impact that chirp might have by extending the constant parameter ξ_0 introduced earlier to an equivalent time-dependent form. Because a chirp in the laser pulse signifies a change of laser frequency with time, the corresponding plasma critical density also becomes time dependent, i.e., $n_c(t) = (n_c)_{\omega_0}\Omega(t)^2$. The chirped CP plane-wave pulse can be considered conceptually as a superposition of all the monochromatic CP plane waves constructed with strength proportional to the instantaneous field envelope and frequency equal to the instantaneous frequency at all times. Hence, the constant parameter ξ_0 also changes and is redefined to its instantaneous form as follows:

$$\xi(t) = \left(\frac{n_e}{n_c}\right)_{\Omega(t)}\frac{d\pi}{\lambda_{\Omega(t)}} = \left(\frac{n_e}{n_c}\right)_{\omega_0}\frac{d\pi}{\lambda}\frac{1}{\Omega(t)} = \frac{\xi_0}{\Omega(t)}. \quad (6)$$

Thus, the ratio relevant to the condition of transparency discussed previously in Sec. II now becomes $\frac{a(t)}{\xi(t)} = \frac{a(t)\Omega(t)}{\xi_0}$.

© Author(s) 2023

The color maps in Fig. 6 plot the value of this ratio for a step target with initial thickness of $d = 0.75\lambda$ and different target peak electron densities at different instants of time. We emphasize here that this oversimplified description does not take into account (among many things) the dynamics of the target, treating the situation as stationary at each time instant. Nevertheless, as we will see, the discussion provides some insight into how the sign of the chirp affects the interaction. Under these conditions, the different cases for negatively chirped ($\zeta = -5$), unchirped ($\zeta = 0$), and positively chirped ($\zeta = +5$) pulses and a step-like target of finite thickness are shown in Fig. 6(d)–Figs. 6(f), respectively.

The main difference between the transparent and opaque regime of operation can be distinguished by the ratio of time-dependent laser pulse amplitude $a(t)$ and the parameter $\xi(t)$. As mentioned in Ref. 38, the condition $a_0/\xi_0 > 1$ indicates the region of operation in relativistic self-induced transparency, and $a_0/\xi_0 \leq 1$ refers to radiation pressure acceleration. Therefore, in Fig. 6(d)–Figs. 6(f), we show the time-dependent ratio of $a(t)$ to $\xi(t)$ as color maps for varying target density (n_e/n_c) and time (t/τ) in order to identify the instant of time (if any) until the peak of the pulse, at which the target reaches the condition of transparency. In our present illustration, the pulse reaches peak amplitude at $t = 0$. We consider the time up to the peak amplitude, i.e., from -8τ to zero to plot the ratio $a(t)/\xi(t)$. Now, to understand the regions of transparency and opacity, we specifically consider the case for a peak density of $6n_c$ shown with a solid horizontal black line along with three important regions marked with contour lines at $a(t)/\xi(t) = 0.7$ in the opaque region, $a(t)/\xi(t) = 1.0$ in the transition or threshold region, and $a(t)/\xi(t) = 1.5$ in the transparent region in Fig. 6(d)–Figs. 6(f).

Before proceeding, we make some observations. First, for the negatively chirped pulse [Fig. 6(d)], because the higher-frequency components of the pulse are interacting at the beginning $(t \leq 0)$, the majority of the field cycles interact up to $t = 0$. By contrast, for the positively chirped pulse [Fig. 6(f)], the low-frequency cycles of the pulse interact with the target initially, therefore the number of field cycles that interact up to the peak $(t \leq 0)$ is much less than in Fig. 6(d). Second, according to the ratio $a(t)/\xi(t)$, at the peak-field instance $(t = 0)$ for the unchirped pulse [Fig. 6(e)] at $n_e = 6n_c$ (horizontal black line), the transparency condition is achieved. By contrast, for the negatively [Fig. 6(d)] and positively [Fig. 6(f)] chirped pulses, the transparency condition is achieved at slightly higher target density (approximately $n_e = 6.25n_c$). Thus, we note that this crossover is before $t = 0$ for the negatively chirped pulse and after $t = 0$ for the positively chirped pulse.

In the real interaction, for the normally incident CP laser pulse, the laser field will propagate dynamically into the target plasma reaching the critical electron density layer before being reflected. From the reflection surface, the light field will penetrate to skin depth and the ponderomotive push of the laser will pile up electrons inside the target, leading to a dynamic in the electron density profile.[64,84] For $\zeta = -5$, the higher-frequency initial part will only start piling up electrons after propagating deeper inside the target compared to the lower-frequency trailing part of the laser. On the other hand, at $\zeta = +5$, the lower-frequency leading part will start spiking the electron density, which when done optimally will reflect the following higher-frequency light more efficiently. Thus, unlike the simplistic picture presented in Fig. 6(d)–Figs. 6(f), in the case of a longer ramp in the target electron density, the laser ponderomotive pressure can be expected to be more effective in the case of $\zeta = +5$ in pushing the electrons out of the target and rendering the target transparent, compared to the case when $\zeta = -5$, because a longer ramp helps the snow-ploughing effect.[72,84] Thus, *a priori*, one might expect less dependence on chirp in the case of step-density targets. In the following, we study this remarkable effect of laser chirp on the previously mentioned step-like foil target having a front density gradient akin to that in Sec. IV.

In Fig. 4(a) and 5(a), we have already discussed the effect of target thickness and density gradient on the transmitted energy fraction in the case of unchirped CP pulses. Now, we expand this idea to chirped laser pulses. Figure 7 shows the transmitted pulse energy fraction for a negatively chirped pulse [Fig. 7(a)] and a positively chirped pulse [Fig. 7(b)] over variable scale lengths and densities. In both cases, two iso-lines are drawn at 2% (black solid) and 40% (black dashed) transmitted laser pulse energy. For the negatively chirped pulse in Fig. 7(a), the threshold density decreases by only ~10% over the entire range of scale length, while compared with Fig. 5(a), the change in threshold density with scale length is minimal. This is evident in the transparent region, where we observe that up to $4n_c$, almost the entire pulse energy is transmitted through the target for all scale lengths ($L = 0$ to 0.8λ). On the other hand, for the positively chirped pulse in Fig. 7(b), at 40% laser energy transmission (black dashed), we see a reduction in threshold density of ~50% for varying target scale length, whereas for the 2% iso-line (black solid), we first observe a decrease of ~14% in target threshold density up to $L = 0.4\lambda$, then from $L = 0.4\lambda$ to 0.8λ, the threshold density increases by nearly 33%. Therefore, the gap between the 2% and 40% transmitted energy fraction iso-lines widens in comparison with the case for the negatively chirped pulse. This effect is due to continuous compression and piling of electrons at the rear side from the low-frequency cycles at the beginning of the interaction with the target, followed by the high-frequency cycles that push them out of the target surface, thereby resulting in continuous transmission of laser energy from the target.

While considering the 2% iso-line, we have observed that one can achieve a higher threshold density in the case of the positively chirped pulse. This implies that experimentally it could be possible to switch the domain of interaction from opaque to transparent just by controlling the chirp parameter. One such contrasting point in the laser–matter parameter space is indicated using the black circles with gray fill in Figs. 7(a) and 7(b) (representing a peak density of $5.6n_c$ and a scale length of 0.7λ). In previous sections, we have observed that over the parameter space of interest in this work, the accelerated ions show quasi-monoenergetic spectral features in the opaque regime of operation, whereas in the transparent regime, the ion spectra have shown flat behavior and sharp cutoffs. Nevertheless, we notice that the bipolar accelerating field generated in the transparent case as shown in Fig. 2(a) shows a nice smooth peak profile located at the exit end of the target ion density profile. This gives us the idea of adding a thin low-density layer at the back of our initial target and seeing whether we can benefit from this accelerating charge separation field and accelerate ions of choice. Therefore, to probe whether the transmitted laser pulse can allow us to accelerate quasi-monoenergetic ions, we add a thin layer (thickness 0.2λ) of low-density $(n_e = 0.1n_c)$ hydrogen behind the

© Author(s) 2023

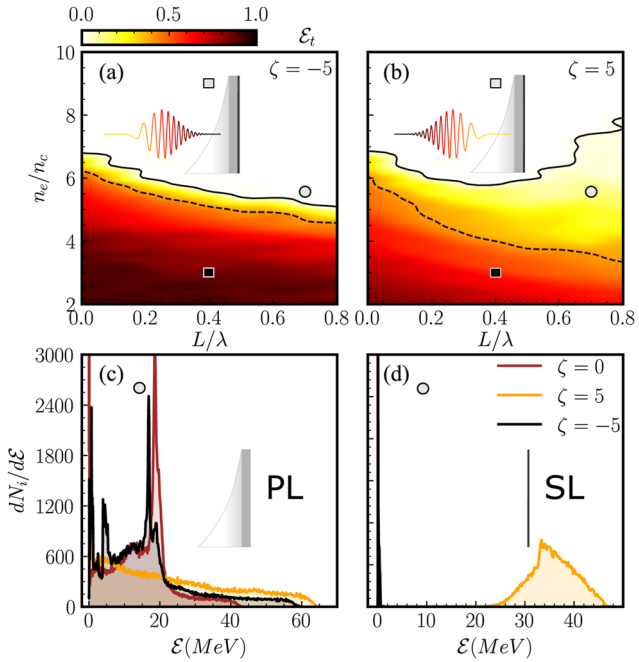

FIG. 7. Upper row: laser pulse transmitted energy fraction $[\mathscr{E}(t)]$ for (a) negatively and (b) positively chirped pulse with varying target density (n_e/n_c) and scale length (L/λ). Similar to the above figures, the iso-lines for transmitted laser energy fraction are marked at 2% (black solid) and 40% (black dashed). The shaded squares (black square with gray fill or the reverse) on the colormap in (a) and (b) indicate the specific transparency conditions corresponding to the primary target electron density. The point marked with the black circle with gray fill in (a) and (b) identifies the target conditions at which the transparency difference due to positive and negative chirp is maximum. Lower row: ion energy spectrum from (c) primary layer (PL) with peak density of $5.6n_c$ and scale length of 0.7λ and (d) secondary layer (SL) with thickness of 0.2λ and density of $0.1n_c$ for unchirped (maroon solid), positively chirped (yellow solid), and negatively chirped (black solid) pulses. The spectra were obtained at a simulation time of 70τ.

main target of thickness 0.75λ. For the main target, we use variable peak densities ($2n_c$ to $10n_c$) and gradient scale lengths (0 to 0.8λ). This results in re-configuring the target geometry to a double-layer target. The parameters for this thin layer are chosen so that the electrostatic field created by the main target layer remains unaltered. In what follows, we refer to the main target as the primary layer (PL) and the additional target as the secondary layer (SL).

In Figs. 7(c) and 7(d), we present the ion energy spectra for the cases of an unchirped pulse ($\zeta = 0$) and positively ($\zeta = 5$) and negatively ($\zeta = -5$) chirped pulses. The respective ion energy spectra from the PL with peak density of $5.6n_c$ and scale length of 0.7λ are shown in Fig. 7(c). In Fig. 7(d), we show the ion energy spectra from the SL with the aforementioned parameters. Here, we choose the PL parameters so that ~20% of the laser pulse energy propagates through the target [see the black circle with gray fill in Figs. 7(a) and 7(b)]. As mentioned previously, in this case, only the positively chirped pulse allows transmission of the laser pulse through the PL. For the negatively chirped and unchirped pulses, the transmission coefficient is close to zero. Previously in Sec. II, we established that in the transmission region, the ion energy spectrum has a near-Maxwellian distribution, whereas a quasi-monoenergetic feature is observed in the opaque region. In Fig. 7(c), we observe similar characteristics of a Maxwellian distribution in the ion energy spectrum for the positively chirped pulse and quasi-monoenergetic features from the negative and unchirped laser pulses. The cutoff ion energy is slightly higher than 60 MeV for the positively chirped pulse and ~60 MeV for the negatively chirped pulse, whereas for the unchirped pulse, the ion cutoff energy is ~40 MeV. Thus, one can utilize chirped pulses to effectively enhance the ion cutoff energy in both regimes (transparency and opacity).

Furthermore, in Fig. 7(d) we show the significance of the SL in the transparency regime. Because only the positively chirped pulse allows the laser to transmit through the PL for a specific set of parameters as indicated in Fig. 7(c), a monoenergetic ion bunch with a peak energy of 35 MeV and a cutoff energy close to 45 MeV is observed. Thus, with an SL and a target with suitable parameters, one can obtain monoenergetic bunches in a controlled manner. By contrast, for the negatively chirped and unchirped pulses, because the PL parameters lie in the opaque region, we observe a clear quasi-monoenergetic spectral signature in the ion spectra from the PL peaking at 20 MeV [Fig. 7(c)] and negligible ion energies from the SL [Fig. 7(d)].

VI. TUNING INTO QUASI-MONOENERGETIC ION SPECTRUM

The key aspect from Sec. V is that by using chirped pulses, one can precisely control the laser transmission through the target with specific properties, or in other words, enhance the threshold density of the target for the incident laser pulse. In Fig. 7(d), we also observed that using an additional layer behind the main target (double-layer target) leads to the generation of monoenergetic ion bunches in the transparency region. Detailed modeling of optimizing the parameters of a double-layer target has been proposed previously in a different context.[8] Here, we keep the configuration of the second layer fixed and look more into the physics aspects. More specifically, to gain further control over the ion energy spectra, we investigate spectral features from both layers independently while controlling the target species and establish the proof of principle.

Toward achieving this goal, we have used a target composed of two layers of different species, i.e., deuterium in the PL and hydrogen in the SL. The target peak densities of the PL are similar to those in Sec. IV, i.e., $n_e = 3n_c$ corresponding to the transparent region and $n_e = 9n_c$ corresponding to the opaque region. Also, the double-layer thicknesses (PL: 0.75λ; SL: 0.2λ) are kept similar to those in Figs. 7(c) and 7(d) with a scale length of $L = 0.4\lambda$. The ion energy spectra are presented in Fig. 8 for an unchirped pulse and positively and negatively chirped pulses, where Figs. 8(a) and 8(c) are for the deuterium target (PL) and Figs. 8(b) and 8(d) are for the hydrogen layer (SL). In Fig. 8(a), we see a spectral signature similar to a Maxwellian distribution, peaking near the cutoff energy as in Fig. 3(e) at 70τ. For the negatively chirped pulse, there is a 50% reduction in ion cutoff energy compared with the positively chirped and unchirped pulses. For this specific set of parameters ($n_e = 3n_c, d = 0.75\lambda, L = 0.4\lambda$), the transmitted energy fraction is substantially higher in the negatively chirp pulse, so the charge separation field cannot be sustained for a

© Author(s) 2023

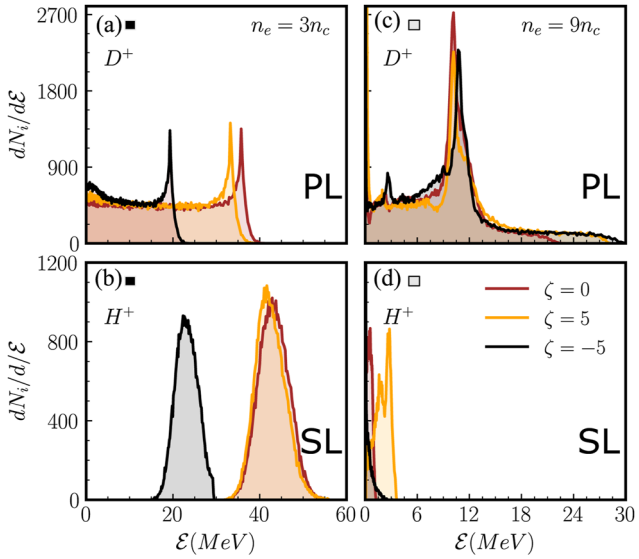

FIG. 8. Ion energy spectra from double-layer target composed of deuterium (PL) and thin (0.2λ) low-density ($0.1n_c$) hydrogen (SL). (a)–(d) show the ion energy spectra from both layers for a PL with a peak electron density of $3n_c$ and $9n_c$, respectively, and with a scale length of 0.4λ in all cases. The colors of the traces indicate the laser chirp conditions: positively chirped (yellow solid), unchirped (maroon solid), and negatively chirped (black solid). The shaded squares (black square with gray fill or the reverse) on the top left corner of each sub-figure correlates with those marked in Figs. 7(a) and 7(b) identifying the transparency conditions corresponding to the primary target electron density.

longer duration to effectively accelerate the ions. On the other hand, the numbers of charged particles being accelerated are almost the same for all three cases.

Figure 8(b) shows the accelerated ion energy spectra from the SL when the density in the PL is $3n_c$. For the negatively chirped pulse, we see prominent monoenergetic ion bunches with a peak energy of ~22.6 MeV and an energy spread of $\Delta\mathcal{E}/\mathcal{E} \sim 28.6\%$. For the positively chirped pulse, the peak energy and energy spread are ~41.7 MeV and $\Delta\mathcal{E}/\mathcal{E} \sim 18.29\%$, and for the unchirped pulse, they are ~43.0 MeV and $\Delta\mathcal{E}/\mathcal{E} \sim 19.8\%$, respectively. The reason behind such monoenergetic behavior in the ion spectra as reconstructed from the PIC simulation results lies in the dynamics of the charge separation field. Figure 8(c) shows the ion energy spectra from the relativistically overdense PL (deuterium), whereas Fig. 8(d) shows the spectra from the SL (hydrogen). The spectra from the PL exhibit similar characteristics to those in Fig. 3(f) for a single-layer target with the same target parameters. In Fig. 8(c), all three cases result in the peak ion energy being at the same position of almost 10 MeV, with different cutoff energies. The maximum ion cutoff energy for the positively and negatively chirped pulses is ~30 MeV, whereas for the unchirped pulse it is ~20 MeV. For this density, the created electrostatic field is much lower than the case for $n_e = 3n_c$, as is evident from Fig. 2(d) in Sec. II for the unchirped pulse with a single target, but this lower electrostatic field remains in the vicinity of the target surface. Because the laser pulse does not transmit through the target under these interaction conditions, low-energy ion bunches were observed from the SL as shown in Fig. 8(d). The maximum ion energy of the bunches reaches 4 MeV only for the positively chirped pulse.

Therefore, note that one can generate quasi-monoenergetic bunches from either the single-layer target in the opaque region or the SL in the transparent region. Also, the spectra give a clear indication about the target species being accelerated.

VII. ION BEAM QUALITY AND INFLUENCE OF LASER FOCUSING ON ACCELERATION REGIMES

To probe the interaction more deeply and to validate our previous observations, we conducted 2D fully relativistic PIC simulations using the WarpX code,[85] in which a Gaussian laser pulse (Gaussian in both space and time) with a wavelength of 1 μm, a duration of 10.0 fs (FWHM of the intensity profile) as in the 1D PIC simulations, and a beam waist ($1/e^2$ of the radius of the intensity spatial profile at focus) of 8 μm was normally incident on a double-layer plasma target. The laser and target conditions were similar to those in Fig. 8, with the PL target comprising deuterium with a thickness of 0.75 μm and the SL comprising hydrogen with a thickness of 0.2 μm. The simulation box was 30×30 μm^2 with the double-layer target located at the center ($x = 0$). The simulations involved a spatial resolution of 170 cells per wavelength and with four ions and six electrons in each dimension. We considered an exponential density ramp with a scale length of 0.4 μm in front of the composite target. For the PL, we considered the two electron densities of $n_e = 3n_c$ and $9n_c$, while that for the SL was $n_e = 0.1n_c$.

Figure 9 shows the 2D PIC simulation results for the transparent (upper panel) and opaque (lower panel) regimes, featuring the ion densities and energy spectra from the PL and SL for an 8 μm focal spot. Figure 9 captures a time snapshot of the process long after the interaction is over, with the laser pulse having already left the simulation box from either the right (post-transmission) or left (post-reflection) side. Figure 9(a) shows clearly that the target ions are expanding with a higher rate in the laser propagation direction, and the SL ions have moved ahead of the PL ions; as is evident, because of the lower mass of ions in the SL, they move faster than those in the PL given the same accelerating field. By contrast, Fig. 9(d) shows that as the laser pulse impinges on the target, the target ions expand from both the front and back surface, and this leads to the formation of a double-peak structure in the ion density profile as in Figs. 1(d)–Figs. 1(d). Although the ions in the SL are lighter in mass, they remain close to the PL ones because they experience a reduced charge separation field at the rear end of the target. This nature of the PL ion density accords with the 1D behavior as seen in Figs. 1(b) and 1(d).

Next, Fig. 9(b) shows the ion energy spectra from both layers (PL and SL) for the relativistic transparency region ($n_e = 3n_c$). In this case, the ions in the PL exhibit a spectral signature similar to a Maxwellian distribution, as in Fig. 8(a) for the unchirped pulse, with a cutoff energy of ~20 MeV. By contrast, the ion spectra from the SL are mono-energetic, peaking at ~24 MeV and with an energy spread of $\Delta\mathcal{E}/\mathcal{E} = 25.9\%$. The ion energies (peak and cutoff) obtained from the 2D PIC simulations are slightly lower than those from the 1D ones, but the 2D ones reproduce qualitatively the characteristics of the ion spectra. Meanwhile, Fig. 9(e) shows the ion energy spectra from the overdense region ($n_e = 9n_c$). Here, from the

© Author(s) 2023

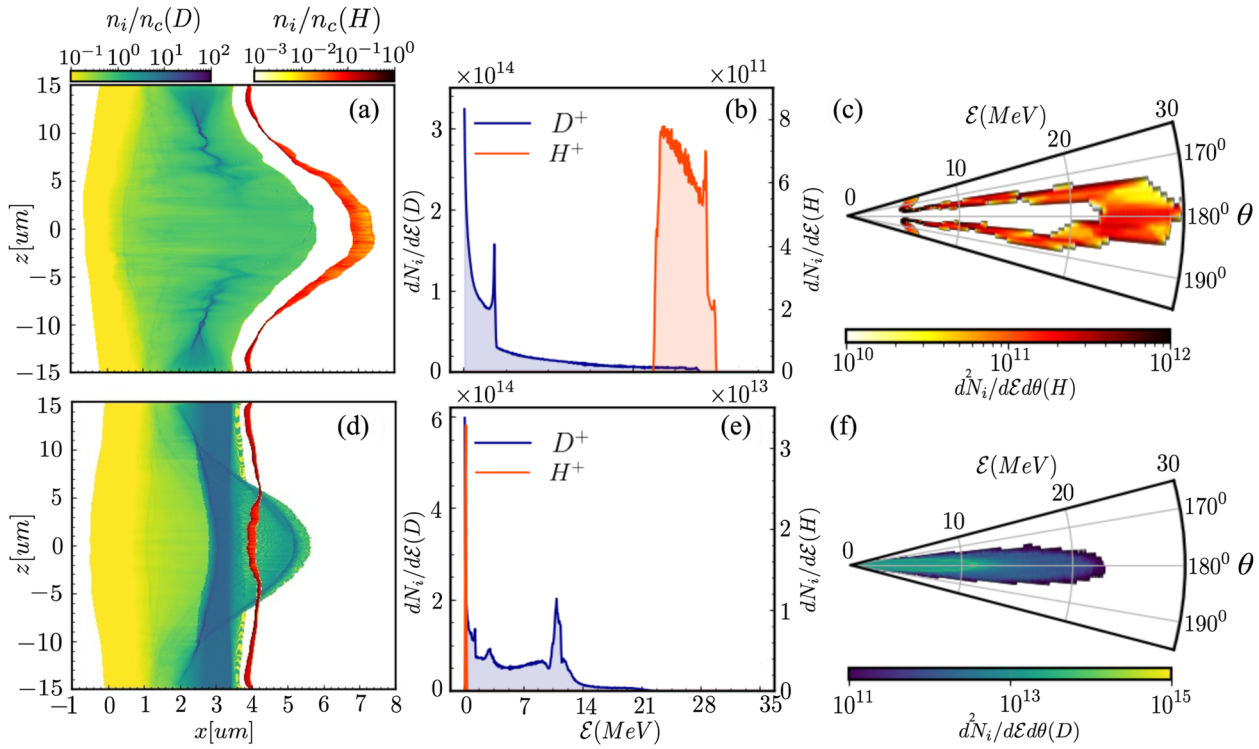

FIG. 9. Target ion density maps for PL (deuterium) and SL (hydrogen) are shown in (a) for $n_e = 3n_c$ (transparency regime) and (d) $n_e = 9n_c$ (reflection regime). The color bars represent the ion densities on a logarithmic scale for both species, in yellow-green for D^+ and yellow-red for H^+. (b) and (e) Ion energy spectrum corresponding to central line outs for $n_e = 3n_c$ and $9n_c$, respectively (PL: deuterium layer in blue and SL: hydrogen layer in orange). The angular energy distribution of the predominant species is shown with the polar plots for both cases in (c) H^+, $3n_c$ and (f) D^+, $9n_c$. The color bar represents the number of ions accelerated at a certain angle with a specific energy in megaelectronvolts. The ion energy 2D spatial distributions and the spectra were obtained at $t = 48.8\tau$, i.e., 24τ after the peak interaction of the laser pulse with the target, similar to the condition in the 1D simulations.

PL we observe a quasi-monoenergetic ion spectrum similar to that in Fig. 8(b) for the unchirped pulse, with a peak energy of ~11 MeV, an energy spread of $\Delta\mathcal{E}/\mathcal{E} = 8.5\%$, and a cutoff energy of 22 MeV, whereas the ions from the SL contribute only a few megaelectronvolts. The ion energy spectra from the overdense region ($n_e = 9n_c$) agree closely with the 1D PIC simulation results as shown in Fig. 8(b) and 8(d).

Figures 9(c) and 9(f) show the polar ion energy spectral map from the target layers to investigate the divergence of the ion beams. Figures 9(c) corresponds to the H^+ ion spectrum shown in Fig. 9(b), whereas Fig. 9(f) corresponds to the D^+ ion spectrum shown in Fig. 9(e). These two simulation cases exhibit monoenergetic and quasi-monoenergetic spectral characteristics. Although the ion divergence in Fig. 9(c) is moderately higher than that in Fig. 9(f), an interesting feature is observed in Fig. 9(c), where ions in the central area (center of the laser focus) accelerate with higher energy compared to those in the peripheral area. This is because ions at the focal center experience higher laser intensity and are pushed by the driver laser at a higher rate under the transparency conditions. Therefore, only the central area of the accelerated ions in Fig. 9(c) can contribute a monoenergetic spectrum, such as shown in Fig. 9(b). By contrast, the ion energies from the D^+ target in the opaque region are those of the low-divergence accelerated ions due to reflection of the driving laser pulse from the target.

For completeness and to verify the dimensional effect in our simulations, we studied the 2D effect on ion acceleration. In 2D simulations, not only does the target incorporate 2D spatial variations but also the driving laser pulse waist is taken into account, so the focal spot plays a crucial role in determining the maximum or cutoff and peak ion energies from the target. Table I summarizes the ion energy cutoff and peak values for the aforementioned target species, density, and thickness with different laser focal spot sizes. As can be seen, in the case of tight focusing (i.e., 4 μm), the ion energies (peak and cutoff) obtained from the PL and SL in the transparent region ($n_e = 3n_c$) are almost half of those obtained with a focal spot size of 8 μm. Similarly, if we treble the focal spot size (i.e., to 12 μm), then the ion energies are ~3 times those with a focal spot size of 4 μm and ~1.5 times those with a focal spot size of 8 μm. Note here that the laser intensity was kept constant throughout, which effectively means increasing laser energy. By contrast, the ion energies in the opaque region ($n_e = 9n_c$) do not change significantly with the focal spot size. This is due to the complete reflection of the laser pulse irrespective of the focal spot size, so the electron dynamics and charge separation field remain almost identical for different focal spot sizes. Compared with the ion energies obtained from the 1D

© Author(s) 2023

TABLE I. Peak and cutoff ion energies obtained in relativistic transparent region ($n_e = 3n_c$) and overdense region ($n_e = 9n_c$) from double-layer target configuration (PL comprising D^+ and SL comprising H^+) with three different driving focal-spot radii ($1/e^2$ of the radius of the intensity spatial envelope at focus), i.e., 4, 8, and 12 μm. Figure 9 summarizes the results for the intermediate focal-spot radius of 8 μm.

Peak density	$n_e = 3n_c$				$n_e = 9n_c$			
Energy (MeV)	Peak		Cutoff		Peak		Cutoff	
Focal-spot radius (μm)	PL (D^+)	SL (H^+)	PL (D^+)	SL (H^+)	PL (D^+)	SL (H^+)	PL (D^+)	SL (H^+)
4	15	13	15	20	9	0.73	21	1.45
8	28	24	28	29	11	0.21	22	0.41
12	41	38	42	45	10.7	0.21	29	0.42

PIC simulations as in Fig. 8, those from the 2D PIC simulations are approximately in the range for a focal spot size of 12 μm, this being because a larger focal spot size (≥12 μm) mimics the laser conditions of 1D simulations near the axis.

VIII. CONCLUSIONS

Herein, we have shown that by tuning accessible petawatt-class laser parameters and target conditions, one can harness the transition between two different acceleration mechanisms, i.e., RIT and RPA, to exert direct control over the ion-bunch spectral features to a large extent. This study enables us to optimize the features of the accelerated ion beams by scanning the target parameters (density, thickness, and geometry), but it also adds additional flexibility via controlling the laser frequency chirp and pre-pulses (to create a suitable pre-plasma). We have shown that the interaction conditions for each of the ion acceleration mechanisms of interest (RIT and RPA) can be identified by analyzing the transmission energy coefficient ($\mathscr{E}_t$) with varying target and laser parameters.

Because of the very different charge particle dynamics in the RIT and RPA regions, the charge separation field generated in the RIT region is substantially stronger than that generated in the opaque region. This leads to considerably different spectral features being generated in the RIT and RPA regions, with Maxwellian-like ion spectra in the RIT region and quasi-monoenergetic ones in the RPA region. We have provided a thorough prescription for how to go from one regime of operation to another and effectively generate quasi-monoenergetic ion spectra. Furthermore, we have established the proof of principle that any chosen ion species can be accelerated to a quasi-monoenergetic energy spectrum under conditions that are realizable and easily controllable in experiments, using a double-layer configuration. The 2D PIC simulations showed clearly the ion acceleration process from different target layers and establish the ion beam quality. Also, the focal spot dimension plays an important role, and the ion energy spectral behavior with larger focal spot agreed with the 1D PIC simulation results.

With the many physical parameters involved, the present numerical study is important for future experimental verification and further extension toward multidisciplinary applications of laser-driven ion beams.[15,16] The possibility of controlling the transition between different ion acceleration mechanisms within the same experimental setup can pave the way to optimizing the ion energies and spectral features depending on the region of operation. Also, the possibility of controlled experiments in this direction might open the door to studying the correlation of ion acceleration with proposed cross-disciplinary studies such as strong-field plasma quantum optics.[86]

ACKNOWLEDGMENTS

This research was supported by the IMPULSE project, which receives funding from the European Union Framework Programme for Research and Innovation Horizon 2020 under Grant Agreement No. 871161. ELI-ALPS is supported by the European Union and co-financed by the European Regional Development Fund (ERDF) (Grant No. GINOP-2.3.6-15-2015-00001). S.K. and S.M. acknowledge Project No. 2020-1.2.4-TÉT-IPARI-2021-00018, which has been implemented with support provided by the National Research, Development and Innovation Office of Hungary and financed under the Grant No. 2020-1.2.4-TET-IPARI-CN funding scheme. S.C.D.M. and S.K. acknowledge the High Performance Computation (HPC) facility/service at ELI-ALPS.

AUTHOR DECLARATIONS

Conflict of Interest

The authors have no conflicts to disclose.

Author Contributions

S.C.D.M. performed the overall calculations, simulations, and post-processing under the guidance of S.K. S.K. conceived the idea and supervised the overall project. S.C.D.M., S.M., and S.K. prepared the final draft with contributions from D.M. All authors participated in the discussions and interpretations of the results.

Shivani Choudhary De Marco: Formal analysis (equal); Investigation (equal); Methodology (supporting); Validation (equal); Visualization (lead); Writing – original draft (equal); Writing – review & editing (equal). **Sudipta Mondal**: Investigation (supporting); Methodology (supporting); Validation (supporting); Writing – original draft (supporting); Writing – review & editing (equal).

© Author(s) 2023

Daniele Margarone: Funding acquisition (supporting); Methodology (supporting); Validation (equal); Writing – review & editing (equal). **Subhendu Kahaly**: Conceptualization (lead); Formal analysis (equal); Funding acquisition (lead); Investigation (equal); Methodology (lead); Supervision (lead); Validation (equal); Visualization (supporting); Writing – original draft (equal); Writing – review & editing (equal).

DATA AVAILABILITY

The data that support the findings of this study are available from the corresponding author upon reasonable request.

REFERENCES

[1]L. Fedeli, A. Formenti, L. Cialfi, A. Pazzaglia, and M. Passoni, "Ultra-intense laser interaction with nanostructured near-critical plasmas," Sci. Rep. **8**, 3834 (2018).

[2]L. Ji, B. Shen, and X. Zhang, "Transparency of near-critical density plasmas under extreme laser intensities," New J. Phys. **20**, 053043 (2018).

[3]F. Sylla, M. Veltcheva, S. Kahaly, A. Flacco, and V. Malka, "Development and characterization of very dense submillimetric gas jets for laser-plasma interaction," Rev. Sci. Instrum. **83**, 033507 (2012).

[4]A. Lifschitz, F. Sylla, S. Kahaly, A. Flacco, M. Veltcheva, G. Sanchez-Arriaga, E. Lefebvre, and V. Malka, "Ion acceleration in underdense plasmas by ultra-short laser pulses," New J. Phys. **16**, 033031 (2014).

[5]S. Kahaly, F. Sylla, A. Lifschitz, A. Flacco, M. Veltcheva, and V. Malka, "Detailed experimental study of ion acceleration by interaction of an ultra-short intense laser with an underdense plasma," Sci. Rep. **6**, 31647 (2016).

[6]J. L. Henares, P. Puyuelo-Valdes, F. Hannachi, T. Ceccotti, M. Ehret, F. Gobet, L. Lancia, J.-R. Marquès, J. J. Santos, M. Versteegen, and M. Tarisien, "Development of gas jet targets for laser-plasma experiments at near-critical density," Rev. Sci. Instrum. **90**, 063302 (2019).

[7]A. Yogo, H. Daido, S. V. Bulanov, K. Nemoto, Y. Oishi, T. Nayuki, T. Fujii, K. Ogura, S. Orimo, A. Sagisaka, J.-L. Ma, T. Z. Esirkepov, M. Mori, M. Nishiuchi, A. S. Pirozhkov, S. Nakamura, A. Noda, H. Nagatomo, T. Kimura, and T. Tajima, "Laser ion acceleration via control of the near-critical density target," Phys. Rev. E **77**, 016401 (2008).

[8]A. Pazzaglia, L. Fedeli, A. Formenti, A. Maffini, and M. Passoni, "A theoretical model of laser-driven ion acceleration from near-critical double-layer targets," Commun. Phys. **3**, 133 (2020).

[9]B. Martinez, E. d'Humières, and L. Gremillet, "Synchrotron radiation from ultrahigh-intensity laser-plasma interactions and competition with Bremsstrahlung in thin foil targets," Phys. Rev. Res. **2**, 043341 (2020); arXiv:2006.16603.

[10]P. Wang, G. Qi, Z. Pan, D. Kong, Y. Shou, J. Liu, Z. Cao, Z. Mei, S. Xu, Z. Liu, S. Chen, Y. Gao, J. Zhao, and W. Ma, "Fabrication of large-area uniform carbon nanotube foams as near-critical-density targets for laser–plasma experiments," High Power Laser Sci. Eng. **9**, e29 (2021).

[11]C. N. Danson, C. Haefner, J. Bromage, T. Butcher, J.-C. F. Chanteloup, E. A. Chowdhury, A. Galvanauskas, L. A. Gizzi, J. Hein, D. I. Hillier, N. W. Hopps, Y. Kato, E. A. Khazanov, R. Kodama, G. Korn, R. Li, Y. Li, J. Limpert, J. Ma, C. H. Nam, D. Neely, D. Papadopoulos, R. R. Penman, L. Qian, J. J. Rocca, A. A. Shaykin, C. W. Siders, C. Spindloe, S. Szatmári, R. M. G. M. Trines, J. Zhu, P. Zhu, and J. D. Zuegel, "Petawatt and exawatt class lasers worldwide," High Power Laser Sci. Eng. **7**, e54 (2019).

[12]C. Radier, O. Chalus, M. Charbonneau, S. Thambirajah, G. Deschamps, S. David, J. Barbe, E. Etter, G. Matras, S. Ricaud, V. Leroux, C. Richard, F. Lureau, A. Baleanu, R. Banici, A. Gradinariu, C. Caldararu, C. Capiteanu, A. Naziru, B. Diaconescu, V. Iancu, R. Dabu, D. Ursescu, I. Dancus, C. A. Ur, K. A. Tanaka, and N. V. Zamfir, "10 PW peak power femtosecond laser pulses at ELI-NP," High Power Laser Sci. Eng. **10**, e21 (2022).

[13]S. Kühn, M. Dumergue, S. Kahaly, S. Mondal, M. Füle, T. Csizmadia, B. Farkas, B. Major, Z. Várallyay, E. Cormier, M. Kalashnikov, F. Calegari, M. Devetta, F. Frassetto, E. Månsson, L. Poletto, S. Stagira, C. Vozzi, M. Nisoli, P. Rudawski, S. Maclot, F. Campi, H. Wikmark, C. L. Arnold, C. M. Heyl, P. Johnsson, A. L'Huillier, R. Lopez-Martens, S. Haessler, M. Bocoum, F. Boehle, A. Vernier, G. Iaquaniello, E. Skantzakis, N. Papadakis, C. Kalpouzos, P. Tzallas, F. Lépine, D. Charalambidis, K. Varjú, K. Osvay, and G. Sansone, "The ELI-ALPS facility: The next generation of attosecond sources," J. Phys. B: At., Mol. Opt. Phys. **50**, 132002 (2017).

[14]D. Charalambidis, V. Chikán, E. Cormier, P. Dombi, J. A. Fülöp, C. Janáky, S. Kahaly, M. Kalashnikov, C. Kamperidis, S. Kühn, F. Lepine, A. L'Huillier, R. Lopez-Martens, S. Mondal, K. Osvay, L. Óvári, P. Rudawski, G. Sansone, P. Tzallas, Z. Várallyay, and K. Varjú, "The extreme light infrastructure—Attosecond light pulse source (ELI-ALPS) project," in *Progress in Ultrafast Intense Laser Science XIII*, *Springer Series in Chemical Physics*, edited by K. Yamanouch (Springer, Cham, 2017), pp. 181–218.

[15]S. Mondal, M. Shirozhan, N. Ahmed, M. Bocoum, F. Boehle, A. Vernier, S. Haessler, R. Lopez-Martens, F. Sylla, C. Sire, F. Quéré, K. Nelissen, K. Varjú, D. Charalambidis, and S. Kahaly, "Surface plasma attosource beamlines at ELI-ALPS," J. Opt. Soc. Am. B **35**, A93 (2018).

[16]D. Margarone, G. Cirrone, G. Cuttone, A. Amico, L. Andò, M. Borghesi, S. Bulanov, S. Bulanov, D. Chatain, A. Fajstavr, L. Giuffrida, F. Grepl, S. Kar, J. Krasa, D. Kramer, G. Larosa, R. Leanza, T. Levato, M. Maggiore, L. Manti, G. Milluzzo, B. Odlozilik, V. Olsovcova, J.-P. Perin, J. Pipek, J. Psikal, G. Petringa, J. Ridky, F. Romano, B. Rus, A. Russo, F. Schillaci, V. Scuderi, A. Velyhan, R. Versaci, T. Wiste, M. Zakova, and G. Korn, "ELIMAIA: A laser-driven ion accelerator for multidisciplinary applications," Quantum Beam Sci. **2**, 8 (2018).

[17]A. Macchi, M. Borghesi, and M. Passoni, "Ion acceleration by superintense laser-plasma interaction," Rev. Mod. Phys. **85**, 751–793 (2013).

[18]J. Schreiber, P. R. Bolton, and K. Parodi, "Invited review article: 'Hands-on' laser-driven ion acceleration: A primer for laser-driven source development and potential applications," Rev. Sci. Instrum. **87**, 071101 (2016).

[19]M. Passoni, F. M. Arioli, L. Cialfi, D. Dellasega, L. Fedeli, A. Formenti, A. C. Giovannelli, A. Maffini, F. Mirani, A. Pazzaglia, A. Tentori, D. Vavassori, M. Zavelani-Rossi, and V. Russo, "Advanced laser-driven ion sources and their applications in materials and nuclear science," Plasma Phys. Controlled Fusion **62**, 014022 (2019).

[20]S. V. Bulanov and V. S. Khoroshkov, "Feasibility of using laser ion accelerators in proton therapy," Plasma Phys. Rep. **28**, 453–456 (2002).

[21]S. V. Bulanov, J. J. Wilkens, T. Z. Esirkepov, G. Korn, G. Kraft, S. D. Kraft, M. Molls, and V. S. Khoroshkov, "Laser ion acceleration for hadron therapy," Phys.-Usp. **57**, 1149–1179 (2014).

[22]L. Karsch, E. Beyreuther, W. Enghardt, M. Gotz, U. Masood, U. Schramm, K. Zeil, and J. Pawelke, "Towards ion beam therapy based on laser plasma accelerators," Acta Oncol. **56**, 1359–1366 (2017).

[23]S. M. Weng, Z. M. Sheng, M. Murakami, M. Chen, M. Liu, H. C. Wang, T. Yuan, and J. Zhang, "Optimization of hole-boring radiation pressure acceleration of ion beams for fusion ignition," Matter Radiat. Extremes **3**, 28–39 (2018), heavy-ion-driven fusion and HEDP (I).

[24]M. Roth, T. E. Cowan, M. H. Key, S. P. Hatchett, C. Brown, W. Fountain, J. Johnson, D. M. Pennington, R. A. Snavely, S. C. Wilks, K. Yasuike, H. Ruhl, F. Pegoraro, S. V. Bulanov, E. M. Campbell, M. D. Perry, and H. Powell, "Fast ignition by intense laser-accelerated proton beams," Phys. Rev. Lett. **86**, 436–439 (2001).

[25]M. Barberio, M. Scisció, S. Vallières, F. Cardelli, S. N. Chen, G. Famulari, T. Gangolf, G. Revet, A. Schiavi, M. Senzacqua, and P. Antici, "Laser-accelerated particle beams for stress testing of materials," Nat. Commun. **9**, 372 (2018).

[26]M. Roth, D. Jung, K. Falk, N. Guler, O. Deppert, M. Devlin, A. Favalli, J. Fernández, D. Gautier, M. Geissel, R. Haight, C. E. Hamilton, B. M. Hegelich, R. P. Johnson, F. Merrill, G. Schaumann, K. Schoenberg, M. Schollmeier, T. Shimada, T. Taddeucci, J. L. Tybo, F. Wagner, S. A. Wender, C. H. Wilde, and G. A. Wurden, "Bright laser-driven neutron source based on the relativistic transparency of solids," Phys. Rev. Lett. **110**, 044802 (2013).

[27]R. A. Snavely, M. H. Key, S. P. Hatchett, T. E. Cowan, M. Roth, T. W. Phillips, M. A. Stoyer, E. A. Henry, T. C. Sangster, M. S. Singh, S. C. Wilks, A. MacKinnon, A. Offenberger, D. M. Pennington, K. Yasuike, A. B. Langdon, B. F. Lasinski, J. Johnson, M. D. Perry, and E. M. Campbell, "Intense high-energy proton beams from petawatt-laser irradiation of solids," Phys. Rev. Lett. **85**, 2945–2948 (2000).

© Author(s) 2023

[28]S. C. Wilks, A. B. Langdon, T. E. Cowan, M. Roth, M. Singh, S. Hatchett, M. H. Key, D. Pennington, A. MacKinnon, and R. A. Snavely, "Energetic proton generation in ultra-intense laser–solid interactions," Phys. Plasmas **8**, 542–549 (2001).
[29]P. Mora, "Plasma expansion into a vacuum," Phys. Rev. Lett. **90**, 185002 (2003).
[30]B. M. Hegelich, B. J. Albright, J. Cobble, K. Flippo, S. Letzring, M. Paffett, H. Ruhl, J. Schreiber, R. K. Schulze, and J. C. Fernández, "Laser acceleration of quasi-monoenergetic MeV ion beams," Nature **439**, 441 (2006).
[31]K. Ogura, M. Nishiuchi, A. S. Pirozhkov, T. Tanimoto, A. Sagisaka, T. Z. Esirkepov, M. Kando, T. Shizuma, T. Hayakawa, H. Kiriyama, T. Shimomura, S. Kondo, S. Kanazawa, Y. Nakai, H. Sasao, F. Sasao, Y. Fukuda, H. Sakaki, M. Kanasaki, A. Yogo, S. V. Bulanov, P. R. Bolton, and K. Kondo, "Proton acceleration to 40 MeV using a high intensity, high contrast optical parametric chirped-pulse amplification/Ti:sapphire hybrid laser system," Opt. Lett. **37**, 2868–2870 (2012).
[32]M. Passoni, L. Bertagna, and A. Zani, "Target normal sheath acceleration: Theory, comparison with experiments and future perspectives," New J. Phys. **12**, 045012 (2010).
[33]F. Kroll, F.-E. Brack, C. Bernert, S. Bock, E. Bodenstein, K. Brüchner, T. E. Cowan, L. Gaus, R. Gebhardt, U. Helbig, L. Karsch, T. Kluge, S. Kraft, M. Krause, E. Lessmann, U. Masood, S. Meister, J. Metzkes-Ng, A. Nossula, J. Pawelke, J. Pietzsch, T. Püschel, M. Reimold, M. Rehwald, C. Richter, H.-P. Schlenvoigt, U. Schramm, M. E. P. Umlandt, T. Ziegler, K. Zeil, and E. Beyreuther, "Tumour irradiation in mice with a laser-accelerated proton beam," Nat. Phys. **18**, 316–322 (2022).
[34]H.-G. Jason Chou, A. Grassi, S. H. Glenzer, and F. Fiuza, "Radiation pressure acceleration of high-quality ion beams using ultrashort laser pulses," Phys. Rev. Res. **4**, L022056 (2022).
[35]N. Iwata, S. Kojima, Y. Sentoku, M. Hata, and K. Mima, "Plasma density limits for hole boring by intense laser pulses," Nat. Commun. **9**, 623 (2018).
[36]A. P. L. Robinson, A. R. Bell, and R. J. Kingham, "Effect of target composition on proton energy spectra in ultraintense laser-solid interactions," Phys. Rev. Lett. **96**, 035005 (2006).
[37]A. P. L. Robinson, M. Zepf, S. Kar, R. G. Evans, and C. Bellei, "Radiation pressure acceleration of thin foils with circularly polarized laser pulses," New J. Phys. **10**, 013021 (2008).
[38]A. Macchi, S. Veghini, and F. Pegoraro, "'Light sail' acceleration reexamined," Phys. Rev. Lett. **103**, 085003 (2009).
[39]A. Macchi, S. Veghini, T. V. Liseykina, and F. Pegoraro, "Radiation pressure acceleration of ultrathin foils," New J. Phys. **12**, 045013 (2010).
[40]W. J. Ma, I. J. Kim, J. Q. Yu, I. W. Choi, P. K. Singh, H. W. Lee, J. H. Sung, S. K. Lee, C. Lin, Q. Liao, J. G. Zhu, H. Y. Lu, B. Liu, H. Y. Wang, R. F. Xu, X. T. He, J. E. Chen, M. Zepf, J. Schreiber, X. Q. Yan, and C. H. Nam, "Laser acceleration of highly energetic carbon ions using a double-layer target composed of slightly underdense plasma and ultrathin foil," Phys. Rev. Lett. **122**, 014803 (2019).
[41]P. Sprangle, E. Esarey, and A. Ting, "Nonlinear theory of intense laser-plasma interactions," Phys. Rev. Lett. **64**, 2011–2014 (1990).
[42]L. Fedeli, A. Formenti, C. E. Bottani, and M. Passoni, "Parametric investigation of laser interaction with uniform and nanostructured near-critical plasmas," Eur. Phys. J. D **71**, 202 (2017).
[43]F. Cattani, A. Kim, D. Anderson, and M. Lisak, "Threshold of induced transparency in the relativistic interaction of an electromagnetic wave with overdense plasmas," Phys. Rev. E **62**, 1234–1237 (2000).
[44]V. V. Goloviznin and T. J. Schep, "Self-induced transparency and self-induced opacity in laser-plasma interactions," Phys. Plasmas **7**, 1564–1571 (2000).
[45]E. Siminos, M. Grech, S. Skupin, T. Schlegel, and V. T. Tikhonchuk, "Effect of electron heating on self-induced transparency in relativistic-intensity laser-plasma interactions," Phys. Rev. E **86**, 056404 (2012).
[46]J. C. Fernández, D. Cort Gautier, C. Huang, S. Palaniyappan, B. J. Albright, W. Bang, G. Dyer, A. Favalli, J. F. Hunter, J. Mendez *et al.*, "Laser-plasmas in the relativistic-transparency regime: Science and applications," Phys. Plasmas **24**, 056702 (2017).
[47]A. A. Sahai, F. S. Tsung, A. R. Tableman, W. B. Mori, and T. C. Katsouleas, "Relativistically induced transparency acceleration of light ions by an ultrashort laser pulse interacting with a heavy-ion-plasma density gradient," Phys. Rev. E **88**, 043105 (2013).
[48]P. L. Poole, L. Obst, G. E. Cochran, J. Metzkes, H.-P. Schlenvoigt, I. Prencipe, T. Kluge, T. Cowan, U. Schramm, D. W. Schumacher, and K. Zeil, "Laser-driven ion acceleration via target normal sheath acceleration in the relativistic transparency regime," New J. Phys. **20**, 013019 (2018).
[49]S. Palaniyappan, B. Manuel Hegelich, H.-C. Wu, D. Jung, D. C. Gautier, L. Yin, B. J. Albright, R. P. Johnson, T. Shimada, S. Letzring, D. T. Offermann, J. Ren, C. Huang, R. Hörlein, B. Dromey, J. C. Fernandez, and R. C. Shah, "Dynamics of relativistic transparency and optical shuttering in expanding overdense plasmas," Nat. Phys. **8**, 763 (2012).
[50]A. Higginson, R. J. Gray, M. King, R. J. Dance, S. D. R. Williamson, N. M. H. Butler, R. Wilson, R. Capdessus, C. Armstrong, J. S. Green, S. J. Hawkes, P. Martin, W. Q. Wei, S. R. Mirfayzi, X. H. Yuan, S. Kar, M. Borghesi, R. J. Clarke, D. Neely, and P. McKenna, "Near-100 MeV protons via a laser-driven transparency-enhanced hybrid acceleration scheme," Nat. Commun. **9**, 724 (2018).
[51]P. K. Singh, F.-Y. Li, C.-K. Huang, A. Moreau, R. Hollinger, A. Junghans, A. Favalli, C. Calvi, S. Wang, Y. Wang, H. Song, J. J. Rocca, R. E. Reinovsky, and S. Palaniyappan, "Vacuum laser acceleration of super-ponderomotive electrons using relativistic transparency injection," Nat. Commun. **13**, 54 (2022); arXiv:2110.13942.
[52]F. Schillaci, L. Giuffrida, M. Tryus, F. Grepl, S. Stancek, A. Velyhan, V. Istokskaia, T. Levato, G. Petringa, G. A. P. Cirrone, J. Cupal, L. Koubiková, D. Peceli, J. A. Jarboe, T. de Castro Silva, M. Cuhra, T. Chagovets, V. Kantarelou, M. Tosca, V. Ivanyan, M. Greplová Žáková, J. Psikal, R. Truneček, A. Cimmino, R. Versaci, V. Olšovlcová, D. Kramer, P. Bakule, J. Ridky, G. Korn, B. Rus, and D. Margarone, "The ELIMAIA laser–plasma ion accelerator: Technological commissioning and perspectives," Quantum Beam Sci. **6**, 30 (2022).
[53]X. Liang, Y. Yi, S. Li, P. Zhu, X. Xie, H. Liu, G. Mu, Z. Liu, A. Guo, J. Kang, Q. Yang, H. Zhu, Q. Gao, M. Sun, H. Lu, Y. Ma, S. Mondal, D. Papp, S. Majorosi, Z. Lécz, A. Andreev, S. Kahaly, C. Kamperidis, N. A. M. Hafz, and J. Zhu, "A laser wakefield acceleration facility using SG-II petawatt laser system," Rev. Sci. Instrum. **93**, 033504 (2022).
[54]N. P. Dover, T. Ziegler, S. Assenbaum, C. Bernert, S. Bock, F.-E. Brack, T. E. Cowan, E. J. Ditter, M. Garten, L. Gaus *et al.*, "Enhanced ion acceleration from transparency-driven foils demonstrated at two ultraintense laser facilities," Light: Sci. Appl. **12**, 71 (2023).
[55]P. Kaw and J. Dawson, "Relativistic nonlinear propagation of laser beams in cold overdense plasmas," Phys. Fluids **13**, 472–481 (1970).
[56]V. A. Vshivkov, N. M. Naumova, F. Pegoraro, and S. V. Bulanov, "Nonlinear electrodynamics of the interaction of ultra-intense laser pulses with a thin foil," Phys. Plasmas **5**, 2727–2741 (1998).
[57]R. Lichters, R. E. W. Pfund, and J. Meyer-ter-Vehn, "LPIC++: A parallel one-dimensional relativistic electromagnetic particle-in-cell code," MPQ Report No. 225, 1997.
[58]S. Choudhary and A. R. Holkundkar, "Efficient ion acceleration by relativistic self-induced transparency in subwavelength targets," Eur. Phys. J. D **70**, 234 (2016).
[59]L. Willingale, P. M. Nilson, A. G. R. Thomas, S. S. Bulanov, A. Maksimchuk, W. Nazarov, T. C. Sangster, C. Stoeckl, and K. Krushelnick, "High-power, kilojoule laser interactions with near-critical density plasma," Phys. Plasmas **18**, 056706 (2011).
[60]L. Obst, S. Göde, M. Rehwald, F.-E. Brack, J. Branco, S. Bock, M. Bussmann, T. E. Cowan, C. B. Curry, F. Fiuza, M. Gauthier, R. Gebhardt, U. Helbig, A. Huebl, U. Hübner, A. Irman, L. Kazak, J. B. Kim, T. Kluge, S. Kraft, M. Loeser, J. Metzkes, R. Mishra, C. Rödel, H.-P. Schlenvoigt, M. Siebold, J. Tiggesbäumker, S. Wolter, T. Ziegler, U. Schramm, S. H. Glenzer, and K. Zeil, "Efficient laser-driven proton acceleration from cylindrical and planar cryogenic hydrogen jets," Sci. Rep. **7**, 10248 (2017).
[61]J. Polz, A. P. L. Robinson, A. Kalinin, G. A. Becker, R. A. Costa Fraga, M. Hellwing, M. Hornung, S. Keppler, A. Kessler, D. Klöpfel, H. Liebetrau, F. Schorcht, J. Hein, M. Zepf, R. E. Grisenti, and M. C. Kaluza, "Efficient laser-driven proton acceleration from a cryogenic solid hydrogen target," Sci. Rep. **9**, 16534 (2019).
[62]A. Sundström, L. Gremillet, E. Siminos, and I. Pusztai, "Collisional effects on the electrostatic shock dynamics in thin-foil targets driven by an ultraintense short pulse laser," Plasma Phys. Controlled Fusion **62**, 085015 (2020).

© Author(s) 2023

[63]I. M. Vladisavlevici, D. Vizman, and E. d'Humières, "Theoretical investigation of the interaction of ultra-high intensity laser pulses with near critical density plasmas," Plasma Phys. Controlled Fusion **65**, 045012 (2023).
[64]A. Macchi, T. V. Liseikina, S. Tuveri, and S. Veghini, "Theory and simulation of ion acceleration with circularly polarized laser pulses," C. R. Phys. **10**, 207–215 (2009).
[65]W. L. Kruer and K. Estabrook, "J×B heating by very intense laser light," Phys. Fluids **28**, 430–432 (1985).
[66]S. Guérin, P. Mora, J. C. Adam, A. Héron, and G. Laval, "Propagation of ultraintense laser pulses through overdense plasma layers," Phys. Plasmas **3**, 2693–2701 (1996).
[67]A. P. L. Robinson, P. Gibbon, M. Zepf, S. Kar, R. G. Evans, and C. Bellei, "Relativistically correct hole-boring and ion acceleration by circularly polarized laser pulses," Plasma Phys. Controlled Fusion **51**, 024004 (2009).
[68]A. P. L. Robinson, R. M. G. M. Trines, N. P. Dover, and Z. Najmudin, "Hole-boring radiation pressure acceleration as a basis for producing high-energy proton bunches," Plasma Phys. Controlled Fusion **54**, 115001 (2012).
[69]S. M. Weng, M. Murakami, P. Mulser, and Z. M. Sheng, "Ultra-intense laser pulse propagation in plasmas: From classic hole-boring to incomplete hole-boring with relativistic transparency," New J. Phys. **14**, 063026 (2012).
[70]A. Pukhov and J. Meyer-ter Vehn, "Laser hole boring into overdense plasma and relativistic electron currents for fast ignition of ICF targets," Phys. Rev. Lett. **79**, 2686 (1997).
[71]P. McKenna, F. Lindau, O. Lundh, D. Neely, A. Persson, and C.-G. Wahlström, "High-intensity laser-driven proton acceleration: Influence of pulse contrast," Philos. Trans. R. Soc., A **364**, 711–723 (2006).
[72]S. Kahaly, S. Monchocé, H. Vincenti, T. Dzelzainis, B. Dromey, M. Zepf, P. Martin, and F. Quéré, "Direct observation of density-gradient effects in harmonic generation from plasma mirrors," Phys. Rev. Lett. **110**, 175001 (2013).
[73]P. Ye, L. Gulyás Oldal, T. Csizmadia, Z. Filus, T. Grósz, P. Jójárt, I. Seres, Z. Bengery, B. Gilicze, S. Kahaly, K. Varjú, and B. Major, "High-flux 100 kHz attosecond pulse source driven by a high-average power annular laser beam," Ultrafast Sci. **2022**, 9823783.
[74]S. Monchocé, S. Kahaly, A. Leblanc, L. Videau, P. Combis, F. Réau, D. Garzella, P. D'Oliveira, P. Martin, and F. Quéré, "Optically controlled solid-density transient plasma gratings," Phys. Rev. Lett. **112**, 145008 (2014).
[75]B. J. Galow, Y. I. Salamin, T. V. Liseykina, Z. Harman, and C. H. Keitel, "Dense monoenergetic proton beams from chirped laser-plasma interaction," Phys. Rev. Lett. **107**, 185002 (2011).
[76]H. Vosoughian, Z. Riazi, H. Afarideh, and E. Yazdani, "Enhancement of proton acceleration by frequency-chirped laser pulse in radiation pressure mechanism," Phys. Plasmas **22**, 073110 (2015).
[77]F. Mackenroth, A. Gonoskov, and M. Marklund, "Chirped-standing-wave acceleration of ions with intense lasers," Phys. Rev. Lett. **117**, 104801 (2016).
[78]S. Choudhary and A. R. Holkundkar, "Chirp assisted ion acceleration via relativistic self-induced transparency," Phys. Plasmas **25**, 103111 (2018).
[79]T. V. Liseikina and A. Macchi, "Features of ion acceleration by circularly polarized laser pulses," Appl. Phys. Lett. **91**, 171502 (2007).
[80]A. Macchi and C. Benedetti, "Ion acceleration by radiation pressure in thin and thick targets," Nucl. Instrum. Methods Phys. Res., Sect. A **620**, 41–45 (2010).
[81]O. Culfa, "Laser-driven particle acceleration at near critical density plasmas," Eur. Phys. J. D **75**, 194 (2021).
[82]M. Almassarani, S. Meng, B. Beleites, F. Ronneberger, G. G. Paulus, and A. Gopal, "Parametric study of proton acceleration from laser-thin foil interaction," Plasma **4**, 670–680 (2021).
[83]B. Gonzalez-Izquierdo, M. King, R. J. Gray, R. Wilson, R. J. Dance, H. Powell, D. A. Maclellan, J. McCreadie, N. M. H. Butler, S. Hawkes, J. S. Green, C. D. Murphy, L. C. Stockhausen, D. C. Carroll, N. Booth, G. G. Scott, M. Borghesi, D. Neely, and P. McKenna, "Towards optical polarization control of laser-driven proton acceleration in foils undergoing relativistic transparency," Nat. Commun. **7**, 12891 (2016).
[84]H. Vincenti, S. Monchocé, S. Kahaly, G. Bonnaud, P. Martin, and F. Quéré, "Optical properties of relativistic plasma mirrors," Nat. Commun. **5**, 3403 (2014).
[85]J.-L. Vay, A. Huebl, A. Almgren, L. D. Amorim, J. Bell, L. Fedeli, L. Ge, K. Gott, D. P. Grote, M. Hogan, R. Jambunathan, R. Lehe, A. Myers, C. Ng, M. Rowan, O. Shapoval, M. Thévenet, H. Vincenti, E. Yang, N. Zaïm, W. Zhang, Y. Zhao, and E. Zoni, "Modeling of a chain of three plasma accelerator stages with the WarpX electromagnetic PIC code on GPUs," Phys. Plasmas **28**, 023105 (2021).
[86]T. Lamprou, R. Lopez-Martens, S. Haessler, I. Liontos, S. Kahaly, J. Rivera-Dean, P. Stammer, E. Pisanty, M. F. Ciappina, M. Lewenstein, and P. Tzallas, "Quantum-optical spectrometry in relativistic laser–plasma interactions using the high-harmonic generation process: A proposal," Photonics **8**, 192 (2021).

© Author(s) 2023